

1           Detection of slow slip events using wavelet  
2           analysis of GNSS recordings

3       Ariane Ducellier<sup>1</sup>, Kenneth C. Creager<sup>2</sup>, and David A. Schmidt<sup>2</sup>

4       <sup>1</sup>Corresponding author. University of Washington, Department of  
5       Earth and Space Sciences, Box 351310, 4000 15th Avenue NE  
6       Seattle, WA 98195-1310

7       <sup>2</sup>University of Washington, Department of Earth and Space  
8       Sciences

9           **Key points**

- 10          • We use a wavelet-based signal processing method to detect transients in  
11        GNSS data, such as slow slip events.
- 12          • In Northern Cascadia, there is good **agreement** between detections of  
13        slow slip using GNSS data and using tremor data.
- 14          • The method **can** be applied **as a starting point to identify slow slip**  
15       **without prior information. New Zealand is shown as on example.**

<sub>16</sub> **Abstract**

<sub>17</sub> In many places, tectonic tremor is observed in relation to slow slip and can  
<sub>18</sub> be used as a proxy to study slow slip events of moderate magnitude where  
<sub>19</sub> surface deformation is hidden in Global Navigation Satellite System (GNSS)  
<sub>20</sub> noise. However, in subduction zones where no clear relationship between tremor  
<sub>21</sub> and slow slip occurrence is observed, these methods cannot be applied, and we  
<sub>22</sub> need other methods to be able to better detect and quantify slow slip. Wavelets  
<sub>23</sub> methods such as the Discrete Wavelet Transform (DWT) and the Maximal  
<sub>24</sub> Overlap Discrete Wavelet Transform (MODWT) are mathematical tools for  
<sub>25</sub> analyzing time series simultaneously in the time and the frequency domain by  
<sub>26</sub> observing how weighted differences of a time series vary from one period to the  
<sub>27</sub> next. In this paper, we use wavelet methods to analyze GNSS time series and  
<sub>28</sub> seismic recordings of slow slip events in Cascadia. We use detrended GNSS  
<sub>29</sub> data, apply the MODWT transform and stack the wavelet details over several  
<sub>30</sub> nearby GNSS stations. As an independent check on the timing of slow slip  
<sub>31</sub> events, we also compute the cumulative number of tremor in the vicinity of the  
<sub>32</sub> GNSS stations, detrend this signal, and apply the MODWT transform. In both  
<sub>33</sub> time series, we can then see simultaneous waveforms whose timing corresponds  
<sub>34</sub> to the timing of slow slip events. We assume that there is a slow slip event  
<sub>35</sub> whenever there is a positive peak followed by a negative peak in the wavelet  
<sub>36</sub> signal. We verify that there is a good **agreement** between slow slip events  
<sub>37</sub> detected with only GNSS data, and slow slip events detected with only tremor  
<sub>38</sub> data for northern Cascadia. The wavelet-based detection method effectively  
<sub>39</sub> detects events of magnitude higher than 6 as determined by independent event  
<sub>40</sub> catalogs (e.g. [Michel et al., 2019]). As a demonstration of using the wavelet  
<sub>41</sub> analysis in a region without significant tremor, we also analyze GNSS data from  
<sub>42</sub> New Zealand and detect slow slip events that are spatially and temporally close

<sup>43</sup> to those detected previously by other studies.

## <sup>44</sup> 1 Introduction

<sup>45</sup> Slow slip events are new phenomena discovered in the last two decades in many  
<sup>46</sup> subduction zones thanks to recordings of the displacement of Earth's surface by  
<sup>47</sup> dense Global Navigation Satellite System (GNSS) networks [Vergnolle et al.,  
<sup>48</sup> 2010, Schmidt and Gao, 2010, Jiang et al., 2012, Wallace et al., 2012]. As with  
<sup>49</sup> ordinary earthquakes, slow slip events represent slip on a fault, for instance  
<sup>50</sup> the plate boundary between a tectonic plate subducting under another tectonic  
<sup>51</sup> plate. However, they take a much longer time (several days to several years) to  
<sup>52</sup> happen relative to ordinary earthquakes. They have a relatively short recurrence  
<sup>53</sup> time (months to years) compared to the recurrence time of regular earthquakes  
<sup>54</sup> (up to several hundreds of years), allowing scientists to observe and study many  
<sup>55</sup> complete event cycles, which is typically not possible to explore with traditional  
<sup>56</sup> earthquake catalogs [Beroza and Ide, 2011]. A slow slip event on the plate  
<sup>57</sup> boundary is inferred to happen when there is a reversal of the direction of motion  
<sup>58</sup> at GNSS stations, compared to the secular interseismic motion. Slow slip  
<sup>59</sup> events have been observed in many places [Beroza and Ide, 2011, Audet and  
<sup>60</sup> Kim, 2016], such as Cascadia [Bartlow, 2020], Nankai [Nishimura et al., 2013],  
<sup>61</sup> Alaska [Li et al., 2016], Costa Rica [Jiang et al., 2012], Mexico [Radiguet  
<sup>62</sup> et al., 2012], and New Zealand [Wallace, 2020].

<sup>63</sup>

<sup>64</sup> In many places, tectonic tremor is also observed in relation to slow slip, but  
<sup>65</sup> the spatial **agreement** between tremor and slow slip may vary along the strike  
<sup>66</sup> of the plate boundary [Hall et al., 2018]. Tremor is a long (several seconds  
<sup>67</sup> to many minutes), low amplitude seismic signal, with emergent onsets, and an  
<sup>68</sup> absence of clear impulsive phases. Tectonic tremor have been explained as a

69 swarm of small, low-frequency earthquakes (LFEs) [Shelly et al., 2007], which  
70 are small magnitude earthquakes ( $M \sim 1$ ) whose frequency content (1-10 Hz) is  
71 lower than for ordinary earthquakes (up to 20 Hz). In subduction zones such as  
72 Nankai and Cascadia, tectonic tremor observations **agree** spatially and tempo-  
73 rally with slow slip observations [Rogers and Dragert, 2003, Obara et al., 2004].  
74 Due to this **agreement**, these paired phenomena have been called Episodic  
75 Tremor and Slip (ETS). However, this is not always the case. For instance, in  
76 northern New Zealand, tremor is more challenging to detect, and seems to be  
77 located downdip of the slow slip on the plate boundary [Todd and Schwartz,  
78 2016]. In Alaska, the tremor zone only partially overlaps the long-term slow  
79 slip zone and there does not appear to be any temporal **agreement** between  
80 tremor and slow slip occurrence [Wech, 2016].

81

82 In Cascadia, there are robust signals in both slow slip and tremor [Hawthorne  
83 and Rubin, 2013]. This is also the case in Nankai [Hiramatsu et al., 2008], where  
84 tiltmeters are used instead of GNSS. It is thus possible to use tremor as a proxy  
85 to observe slow slip events that are not directly observed in the GNSS data.  
86 For instance, Aguiar et al. [2009] studied 23 ETS events in Cascadia with more  
87 than 50 hours of tectonic tremor. For all these events, they computed both the  
88 GPS-estimated moment release and the cumulative number of hours of tectonic  
89 tremor recorded. They observed a linear relationship between moment release  
90 and number of hours of tremor for slow slip events of moment magnitude 6.3  
91 to 6.8. Based on this linear relationship, it is possible to infer the existence of  
92 smaller slow slip events of magnitude 5-6 occurring simultaneously with smaller  
93 tremor bursts of duration 1 to 50 hours occurring in between the big ETS events,  
94 and for which there is no detectable signal in the GPS data.

95

96        Frank [2016] divided GPS time series observations from Cascadia and Guer-  
97        rero, Mexico, into two groups: the first group contains days with abundant  
98        tremor and LFEs, the second group contains days when the number of tremor  
99        or LFEs is lower than a threshold. He then stacked separately the two groups  
100       of daily observations and observed a cumulative displacement in the direction  
101       corresponding to the loading period when few tremor or LFEs are observed  
102       and the surface deformation corresponds to the secular plate motion. He also  
103       observed a cumulative displacement in the opposite direction corresponding to  
104       the release period when tremor and LFEs are observed. He was thus able to  
105       observe a reverse displacement corresponding to smaller slow slip events not  
106       directly observable in the GPS data for individual events.

107

108       However, these methods cannot be applied to detect slow slip events in places  
109       where tremor and slow slip occurrence are not well spatially and temporally cor-  
110       related, tremor is not abundant, or the seismic network is not robust enough.  
111       We thus need other methods to be able to better detect and quantify slow slip.

112

113       Wavelet methods such as the Discrete Wavelet Transform (DWT) are math-  
114       ematical tools for analyzing time series simultaneously in the time and the fre-  
115       quency domain by observing how weighted differences of a time series vary from  
116       one period to the next. Wavelet methods have been widely used for geophysical  
117       applications (e.g. Kumar and Foufoula-Georgiou [1997]). However, few studies  
118       have used wavelet methods to analyze recordings of slow slip, and their scope  
119       was limited to the detection of the bigger (magnitude 6-7) short-term (a few  
120       weeks) events [Szeliga et al., 2008, Ohtani et al., 2010, Wei et al., 2012, Alba  
121       et al., 2019].

122

123 Szeliga et al. [2008] determined the timing and the amplitude of 34 slow  
124 slip events throughout the Cascadia subduction zone between 1997 and 2005  
125 using wavelets. They modeled the GPS time series by the sum of a linear trend,  
126 annual and biannual sinusoids representing seasonal effects, Heaviside step func-  
127 tions corresponding to earthquakes and hardware upgrades, and a residual sig-  
128 nal. They then applied a Gaussian wavelet transform to the residual time series  
129 to get the exact timing of slow slip at each GPS station. The idea is that the  
130 wavelet transform allows us to analyze the signal both in the time and the fre-  
131 quency domains. A sharp change in the signal will be localized and seen at all  
132 time scales of the wavelet decomposition, contrary to what happens with the  
133 periodic sinusoids of the Fourier transform.

134

135 Instead of using wavelets in the time domain, Ohtani et al. [2010] used 2D  
136 wavelet functions in the spatial domain to detect slow slip events. They de-  
137 signed the Network Stain Filter (NSF) to detect transient deformation signals  
138 from large-scale geodetic arrays. They modeled the position of the GPS station  
139 by the sum of the secular velocity, a spatially coherent field, site-specific noise,  
140 reference frame errors, and observation errors. The spatial displacement field is  
141 modeled by the sum of basis wavelets with time-varying weights. Their method  
142 has been successfully used to detect a transient event in the Boso peninsula,  
143 Japan, and a slow slip event in the Alaska subduction zone [Wei et al., 2012].

144

145 Finally, Alba et al. [2019] used hourly water level records from four tide  
146 gauges in the Juan de Fuca Straight and the Puget Sound to determine relative  
147 vertical displacements associated with slow slip events between 1996 and 2011.  
148 Their main idea is that the tidal level measured at a given gauge is the sum of  
149 a noise component at multiple timescales (tides, ocean and atmospheric noise)

150 and an uplift signal due to the slow slip events. The noise component is assumed  
151 to be coherent between all tidal gauges, while the tectonic uplift signal is differ-  
152 ent provided that the gauges are far enough from each other. By stacking the  
153 tidal records after removing tides, the uplift signals cancel each other while the  
154 noise signal is amplified. By stacking the components at different time scales of  
155 the DWT decomposition, instead of stacking the raw tidal record, each of the  
156 components of the noise at different time scales is retrieved and can then be  
157 removed from the raw records to obtain the uplift signal. Due to the relative  
158 location of the tidal gauges at Port Angeles and Port Townsend compared to the  
159 slow slip region on the plate boundary, a slow slip event should result in uplift  
160 in Port Angeles (western part) and in subsidence in Port Townsend (eastern  
161 part). Indeed, the authors were able to clearly see a difference in the sign of the  
162 uplift at these two tidal gauges.

163

164 In our study, we use a similar approach to previous studies with a different  
165 reasoning. We only stack signals at nearby GPS stations, assuming that the  
166 east-west displacement due to the slow slip events will then be the same at each  
167 of the GPS stations considered. We suppose that some of the noise component  
168 is different at each GPS station and will be eliminated by the stacking. Finally,  
169 we assume that the noise and the longitudinal displacement due to the slow  
170 slip events and the secular plate motion have different time scales, so that the  
171 wavelet decomposition will act as a bandpass filter to retrieve the displacement  
172 signal and highlight the slow slip events. We use wavelet methods to analyze  
173 GPS and tremor recordings of slow slip events in Cascadia. Our objective is to  
174 verify that there is a good **agreement** between slow slip events detected with  
175 only GNSS data, and slow slip events detected with only tremor data. We thus  
176 want to demonstrate that the wavelet-based detection method can be applied to

177 detect slow slip events that may currently be obscured using standard methods.  
178 Finally, we apply the method to GNSS data in New Zealand and successfully  
179 detect several slow slip events without needing to rely on the tremor data.

180

## 181 2 Data

182 We first focused our study on northwest Washington State. For the GNSS data,  
183 we used the GPS time series provided by the Pacific Northwest Geodetic Ar-  
184 array, Central Washington University. These are network solutions in ITRF2014  
185 with phase ambiguities resolved with wide-lane phase-biases. Orbit and satel-  
186 lite clocks provided by the Jet Propulsion Laboratory/NASA. North, East, and  
187 Vertical directions are available. However, as the direction of the secular plate  
188 motion is close to the East direction, we only used the East direction of the GPS  
189 time series for the data analysis, as it has the best signal-to-noise ratio. The  
190 wavelet method works best with data with zero mean, and no sharp discontinu-  
191 ities; so we use the cleaned dataset, that is GPS times series with linear trends,  
192 steps due to earthquakes or hardware upgrades, and annual and semi-annual  
193 sinusoids signals simultaneously estimated and removed following Szeliga et al.  
194 [2004]. For the tremor data, we used the tremor catalog from the Pacific North-  
195 west Seismic Network (PNSN) [Wech, 2010].

196

197 For the application to slow slip events in New Zealand, we used the GPS  
198 time series provided by the Geological hazard information for New Zealand  
199 (GeoNet). The coordinates have been extracted by GeoNet during the GLOBK  
200 run from the combined daily solution files, and converted to (east, north, up)  
201 displacement in millimeters with respect to an a priori position and epoch in the  
202 ITRF2008 realization. The time series provided by GeoNet have no adjustments

made to them, so they may, for example, contain offsets due to earthquakes, offsets due to equipment changes at individual sites, and seasonal (annual and semi-annual) signals due to various causes. Here again, the direction of the secular interseismic plate motion is close to the West direction, so we only used the East-West component of the GPS time series for the data analysis. We detrended the data before applying the wavelet transform by carrying a linear regression of the whole time series and removing the straight line obtained from the regression.

### 3 Method

#### 3.1 The Maximal Overlap Discrete Wavelet Transform

The Discrete Wavelet Transform (DWT) is an orthonormal transform that transforms a time series  $X_t$  ( $t = 0, \dots, N - 1$ ) into a vector of wavelet coefficients  $W_i$  ( $i = 0, \dots, N - 1$ ). If we denote  $J$  the level of the wavelet decomposition, and the number of observations is equal to  $N = n * 2^J$ , where  $n$  is some integer greater than or equal to 1, the vector of wavelet coefficients can be decomposed into  $J$  wavelet vectors  $W_j$  of lengths  $\frac{N}{2}, \frac{N}{4}, \dots, \frac{N}{2^J}$ , and one scaling vector  $V_J$  of length  $\frac{N}{2^J}$ . Each wavelet vector  $W_j$  is associated with changes on time scale  $\tau_j = dt2^{j-1}$ , where  $dt$  is the time step of the time series, and corresponds to the filtering of the original time series with a filter with nominal frequency interval  $[\frac{1}{dt2^{j+1}}; \frac{1}{dt2^j}]$ . The scaling vector  $V_J$  is associated with averages in time scale  $\lambda_J = dt2^J$ , and corresponds to the filtering of the original time series with a filter with nominal frequency interval  $[0; \frac{1}{dt2^{j+1}}]$ . Wavelet vectors can be further decomposed into details and smooths, which are more easily interpretable. We define for  $j = 1, \dots, J$  the  $j$ th wavelet detail  $D_j$ , which is a vector of length  $N$ , and is associated to time scale  $\tau_j = dt2^{j-1}$ . Similarly, we can

228 define for  $j = 1, \dots, J$  the  $j$ th wavelet smooth  $S_j$ , which is a vector of length  
 229  $N$ , and is associated to scales  $\tau_{j+1} = dt2^{j+1}$  and higher. The basic idea is to  
 230 reapply to  $W_j$  the wavelet filter that was used to construct  $W_j$  from the initial  
 231 time series  $X$ . Together, the details and the smooths define the multiresolution  
 232 analysis (MRA) of  $X$ :

$$233 \quad X = \sum_{j=1}^J D_j + S_J \quad (1)$$

234 The DWT presents several disadvantages. First, the length of the time se-  
 235 ries must be a multiple of  $2^J$  where  $J$  is the level of the DWT decompositon.  
 236 Second, the time step of the wavelet vector  $W_j$  is  $dt2^j$ , which may not corre-  
 237 spond to the time when some interesting phenomenon is visible on the original  
 238 time series. Third, when we circularly shift the time series, the corresponding  
 239 wavelet coefficients, details and smooths are not a circularly shifted version of  
 240 the wavelet coefficients, details and smooths of the original time series. Thus,  
 241 the values of the wavelet coefficients, details and smooths are strongly dependent  
 242 on the time when we start experimentally gathering the data. Finally, when we  
 243 filter the time series to obtain the details  $D_j$  and smooths  $S_j$ , we introduce a  
 244 phase shift, which makes it difficult to line up meaningfully the features of the  
 245 MRA with the original time series.

246  
 247 To overcome the disadvantages described above, we use instead the Maxi-  
 248 mal Overlap Discrete Wavelet Transform (MODWT). The MODWT transforms  
 249 the time series  $X_t$  ( $t = 0, \dots, N - 1$ ) into  $J$  wavelet vectors  $\tilde{W}_j$  ( $j = 1, \dots, J$ ) of  
 250 length  $N$  and a scaling vector  $\tilde{V}_J$  of length  $N$ . As is the case for the DWT,  
 251 each wavelet vector  $\tilde{W}_j$  is associated with changes on scale  $\tau_j = dt2^{j-1}$ , and  
 252 corresponds to the filtering of the original time series with a filter with nominal  
 253 frequency interval  $[\frac{1}{dt2^{j+1}}, \frac{1}{dt2^j}]$ . The scaling vector  $\tilde{V}_J$  is associated with aver-

254      ages in scale  $\lambda_J = dt2^J$ , and corresponds to the filtering of the original time  
 255      series with a filter with nominal frequency interval  $[0; \frac{1}{dt2^{J+1}}]$ . As is the case for  
 256      the DWT, we can write the MRA:

$$257 \quad X = \sum_{j=1}^J \tilde{D}_j + \tilde{S}_J \quad (2)$$

258      The MODWT of a time series can be defined for any length  $N$ . The time  
 259      step of the wavelet vectors  $\tilde{W}_j$  and the scaling vector  $\tilde{V}_J$  is equal to the time  
 260      step of the original time series. When we circularly shift the time series, the  
 261      corresponding wavelet vectors, scaling vector, details and smooths are shifted  
 262      by the same amount. The details and smooths are associated with a zero phase  
 263      filter, making it easy to line up meaningfully the features of the MRA with the  
 264      original time series. The wavelet methods for time series analysis are explained  
 265      in a more detailed way in [Percival and Walden, 2000]).

266

267      **The boundary conditions at the two edges of the time series will**  
 268      **affect the wavelet coefficients.** For the MODWT, if we denote  $L$  the  
 269      length of the base wavelet filter used for the wavelet decomposition  
 270      (in our study, we used a Least Asymmetric wavelet filter of length  
 271       $L = 8$ , see [Percival and Walden, 2000], section 4.8, page 107), the  
 272      length of the wavelet filter at level  $j$  used to compute the wavelet  
 273      detail  $D_j$  is:

$$L_j = (2^j - 1)(L - 1) + 1$$

274      The wavelet coefficients of the detail al level  $j$  affected by the  
 275      boundary conditions at the edges would then be the coefficients with  
 276      indices  $t = 0, \dots, L_j - 2$  or  $t = N - L_j + 1, \dots, N - 1$  (see [Percival and

277 Walden, 2000], section 5.11, page 199). We get  $L_j = 442$  for  $j = 6$ ,  
278  $L_j = 890$  for  $j = 7$  and  $L_j = 1786$  for  $j = 8$ . In practice, the part  
279 of the wavelet details affected by the boundary conditions is much  
280 shorter than that. We compared the wavelet details computed when  
281 using only the data between 2008 and 2012 and the wavelet details  
282 computed when using the entire time series from 2000 to 2021 (Figure  
283 S1 in the Supplementary Material). Even at level 8 only about 6  
284 months of data on each side are effected by the boundary conditions.

285 **3.2 Application to synthetic data**

286 To illustrate the wavelet transform method, we first apply the MODWT to syn-  
287 synthetic data. As slow slip events occur in Cascadia on a regular basis, every  
288 twelve to eighteen months, we create a synthetic signal of period  $T = 500$  days.  
289 To reproduce the ground displacement observed on the longitudinal component  
290 of GPS stations in Cascadia, we divide each period into two parts: In the first  
291 part of duration  $T - N$ , the displacement is linearly increasing and corresponds  
292 to the inter seismic plate motion in the eastern direction; in the second part  
293 of duration  $N$ , the displacement is linearly decreasing and corresponds to a  
294 slow slip event on a reverse fault at depth triggering a ground displacement in  
295 the western direction. To see the effect of the duration of the slow slip event,  
296 we use different values for  $N = 5, 10, 20, 40$  days. The amplitude of the set is  
297 normalized to 1. Figure 1 shows the synthetics, the details  $D_j$  of the wavelet  
298 decomposition for levels 1 to 10, and the smooth  $S_{10}$  for the four durations of a  
299 slow slip event.

300  
301 The ramp-like signal is transformed through the wavelet filtering into a wave-  
302 form with first a positive peak and then a negative peak. The shape of the wave-

303 form is the same for every level of the wavelet decomposition, but the width of  
304 the waveform increases with the scale level. For the 8th level of the wavelet de-  
305 composition, the width of the waveform is nearly as large as the time between  
306 two events. At larger scales, the waveforms start to merge two contiguous events  
307 together, and make the wavelet decomposition less interpretable. For an event  
308 of duration 5 days, the wavelet details at levels higher than 3 have a larger  
309 amplitude than the wavelet details at lower scales. For an event of duration 10  
310 days, the wavelet details at levels higher than 4 have a larger amplitude than  
311 the wavelet details at lower scales. For an event of duration 20 days, the wavelet  
312 details at levels higher than 5 have a larger amplitude than the wavelet details  
313 at lower scales. For an event of duration 40 days, the wavelet details at levels  
314 higher than 6 have a larger amplitude than the wavelet details at lower scales.  
315 Thus, the scale levels at which an event is being seen in the wavelet details give  
316 us an indication about the duration (and the magnitude) of the slow slip event.  
317 The big slow slip events of magnitude 6-7 typically trigger a signal that lasts  
318 about one week at an individual GPS station, and the whole event lasts several  
319 weeks. We expect them to start being visible at the level 5 of the wavelet de-  
320 composition, but to not be noticeable at lower time scales.

321

### 322 3.3 MODWT of GPS and tremor data

323 The DWT and MODWT methods must be used on a continuous time series,  
324 without gaps in the recordings. To deal with the gaps in the GNSS recordings,  
325 we simply replace the missing values by interpolation. The value for the first  
326 day for which data are missing is equal to the mean of the five days before  
327 the gap. The value for the last day for which data are missing is equal to the  
328 mean of the five days after the gap. The remaining missing values are com-

puted by doing a linear interpolation of the first and the last values and adding a Gaussian noise component with mean zero and standard deviation equal to the standard deviation of the whole time series. We verify how the wavelet details may be affected by looking at a GPS time series without missing values and compared the wavelet details with and without removing some data points. Station PGC5 recorded continuous 1390 days between 2009 and 2013 without any missing values. We first computed the wavelet details without missing values. Then, we removed ten neighboring values, replaced them using the method described above (linear interpolation plus Gaussian noise), and computed the wavelet details with the replaced values. Figure S2 in the Supplementary Material shows a comparison of the two wavelet details for two different locations of the missing values. We can see that there are visible differences in the time series itself, and in the details at the smallest levels of the wavelet decomposition. However, the differences between the wavelet details with and without missing values get smaller and smaller with increasing levels of details, and are barely visible for the levels that are most relevant (levels 6 and above). We thus conclude that we can easily replace the missing values in the GNSS time series without introducing false detections of slow slip events.

We then applied the wavelet filtering to real GPS data. Figure 2 shows the longitudinal displacement for GPS station PGC5, located in southern Vancouver Island, the details of the wavelet decomposition for levels 1 to 8, and the smooth. In the data, we can see a sharp drop in displacement whenever there is a documented slow slip event. For levels 5 to 8, which correspond to time scales 16, 32, 64 and 128 days, we can see in the details a positive peak followed by a negative peak whenever there is a drop in displacement in the data. We thus verify that the wavelet method can detect steps in the time series associated

356 with slow slip events.

357

358 To increase the signal-to-noise ratio and better detect slow slip events, we  
359 stack the signal from several neighboring GPS stations. We choose to focus on  
360 GPS stations located close enough to the tremor zone to get a sufficiently high  
361 amplitude of the slow slip signal. We choose 16 points along the 40 km depth  
362 contour of the plate boundary (model from Preston et al. [2003]) with spacing  
363 equal 0.1 degree in latitude (red triangles on Figure 3). Then we took all the  
364 GPS stations located in a 50 km radius for a given point, compute the wavelet  
365 details for the longitudinal displacement of each station, and stack each detail  
366 over the GPS stations. We thus have a stacked detail for each level 1 to 10 of  
367 the wavelet decomposition.

368

369 To assess the success of the wavelet decomposition for detecting slow slip  
370 events in GPS time series, we validate the approach by comparing to an inde-  
371 pendent proxy for slow slip events. We took all the tremor epicenters located  
372 within a 50 km radius centered on one of the 16 locations marked by red trian-  
373 gles on Figure 3. Then we computed the cumulative number of tremor within  
374 this circle. Finally, we removed a linear trend from the cumulative tremor count,  
375 and applied the wavelet transform. Because of the preprocessing applied to the  
376 tremor data before that wavelet transform, **the measurement unit associ-**  
377 **ated with the corresponding wavelet details is the fraction of tremor**  
378 **in a day divided by the total number of days. The average value is**  
379 **1 divided by the total number of days.** Figure 4 shows an example of the  
380 wavelet decomposition for the third northernmost location on Figure 3 (which  
381 is closest to GPS station PGC5). Contrary to what happens for the GPS data,  
382 we see a sharp increase in the time series whenever there is a tremor episode,

383 which translates into a negative peak followed by a positive peak in the wavelet  
384 details.

## 385 4 Application to data from Cascadia

386 We stacked the 8th level detail of the wavelet decomposition of the displacement  
387 over all the GPS stations located in a 50 km radius of a given point, for the 16  
388 locations indicated in Figure 3. The result is shown in the top panel of Figure 5,  
389 where each line represents one of the locations along strike. To better highlight  
390 the peaks in the wavelet details, we highlighted in red the time intervals where  
391 the amplitude of the stacked detail is higher than a threshold, and in blue the  
392 time intervals where the amplitude of the stacked detail is lower than minus the  
393 threshold. To compare the GPS signal with the tremor signal, we plotted the  
394 8th level detail of the wavelet decomposition of the tremor count on the bottom  
395 panel of Figure 5. We multiplied by -1 the cumulative tremor count for the  
396 wavelet decomposition in order to be able to match positive peaks with positive  
397 peaks and negative peaks with negative peaks. In the tremor catalog from the  
398 PNSN, there are 17 tremor events with more than 150 hours of tremor recorded.  
399 The events are summarized in Table 1. The time of the event is the start date  
400 plus half the duration of the event.

401

402 Although the latitudinal extension of the events is not always the same for  
403 the GPS data and for the tremor data, we identify the same 13 events in both 8th  
404 wavelet decompositions for the 8th level: January 2007, May 2008, May 2009,  
405 August 2010, August 2011, September 2012, September 2013, August-November  
406 2014, January 2016, March 2017, June 2018, March-November 2019, and Oc-  
407 tober 2020-January 2021. Although there are two events in the tremor catalog  
408 in August 2014 and November 2014, these two events are not distinguishable in

409 the 8th level details and look more like a single event slowly propagating from  
410 South to North. The same phenomenon is observed in 2019 when two tremor  
411 events in March and November 2019 are merged into a single event propagating  
412 slowly from South to North. In 2020-2021, the wavelet decomposition of the  
413 tremor shows one event in the south in October-November 2020 and one event  
414 in the North in January 2021, but in the wavelet decomposition of the GPS  
415 data, these three events look like a single event propagating slowly from South  
416 to North.

417

418 A similar comparison is shown for the wavelet decomposition of the GPS  
419 data and the wavelet decomposition of the tremor count data for the 7th level  
420 and the 6th level respectively (Figures 6 and 7). The events are harder to see in  
421 the 7th level than in the 8th level, both for the GPS data and the tremor count  
422 data. The wavelet decomposition is more noisy for the GPS data between 2010  
423 and 2012, but it does not seem that there are more slow slip events visible in  
424 the 7th level.

425

426 For the 6th level detail, we see an additional event in the South in Fall 2009  
427 that is present both in the GPS and the tremor data. It may correspond to the  
428 northern extent of a big ETS event occurring in Fall 2009 south of the study  
429 area (event 19 in the Michel et al. [2019] catalog). There are three small sig-  
430 nals in the GPS data in Winter 2012, Fall 2017, and Winter 2020 that are not  
431 present in the tremor data, and may be false detections. To summarize, we  
432 assume that robust detections are events present in both GPS and tremor time  
433 series, and false detections are events present in the GPS but not in the tremor  
434 time series. Then, all the 13 events present on the 8th level detail of the wavelet  
435 decomposition are robust detections and 14 of the 17 events present on the 6th

436 level detail of the wavelet decomposition are robust detections.

437

438 To better evaluate the number of robust and false detections, we convert  
439 the wavelet details into trinary time series. If the absolute value of the wavelet  
440 detail is higher than a threshold, we replace the value by 1 (for positive values)  
441 or -1 (for negative values), otherwise we replace the value by 0. We do this  
442 on both the wavelet details of the GPS data and of the tremor data. Then we  
443 decide that if both the GPS and the tremor time series take the value 1 (or  
444 both take the value -1), we have a robust detection (true positive, TP). If the  
445 GPS and the tremor time series have opposite signs, or if the absolute value of  
446 the GPS time series is 1 but the value of the tremor time series is 0, we have a  
447 false detection (false positive, FP). If both time series take the value 0, we do  
448 not have detection (true negative, TN). If the GPS time series take the value  
449 0, but the absolute value of the tremor time series is 1, we miss a detection  
450 (false negative, FN). We then define the sensitivity (true positive rate) and the  
451 specificity (equal to 1 minus the false positive rate) as:

$$\begin{aligned} \text{sensitivity} &= \frac{TP}{TP + FN} \\ \text{specificity} &= \frac{TN}{TN + FP} \end{aligned} \quad (3)$$

452 We can then evaluate the quality of the detections obtained with our method  
453 by plotting a receiver operating characteristic curve (ROC curve). The ROC  
454 curve is widely used for binary classification problems in statistics and machine  
455 learning. We calculate an ROC value by varying the values of the threshold  
456 (here the two thresholds used to convert the GPS and the tremor time series  
457 into trinary time series), computing the corresponding values of the true positive  
458 rate and the false positive rate (equal to 1 minus the specificity), and plotting  
459 the true positive rate as a function of the false positive rate. If the classifica-

460 tion was made randomly, all the points would fall on the first diagonal. If the  
461 classifier was perfect, the corresponding point would fall on the top left cor-  
462 ner of the graph with true positive rate equal to 1 and false positive rate equal  
463 to 0. The bigger the area under the curve, the better the classification method is.

464

465 As the slow slip events are better seen on levels 6, 7 and 8 of the wavelet  
466 decomposition, we first add the wavelet details corresponding to levels 6 to 8,  
467 and transform the resulting time series into a trinary time series. We apply this  
468 transform to both the GPS and the tremor time series with varying thresholds.  
469 We then plot the ROC curve on Figure 8, each dot representing a different  
470 threshold. The corresponding sums of the wavelet details for the GPS data and  
471 the tremor data are shown on Figure 9. We can see that there is a trade-off  
472 between sensitivity and specificity as we vary the threshold. If we decrease the  
473 false positive rate, we also decrease the number of true events detected. If we  
474 increase the number of true events detected, we also increase the false positive  
475 rate. If we increase the threshold for the tremor, the curve goes farther away  
476 from the first diagonal, that is we get better classification results. If we increase  
477 the threshold for the GPS, the false positive rate and the the number of events  
478 detected decrease. In Figure 9, we have chosen thresholds for the GPS time  
479 series and the tremor time series such that the specificity is higher than 0.75  
480 (that is the false positive rate is lower than 0.25), and the sensitivity is the  
481 highest possible, that is we have chosen the thresholds corresponding to the dot  
482 that is farthest from the diagonal, which is random.

483

484 In addition to the magnitude 6 events discussed above, Michel et al. [2019]  
485 have also identified several magnitude 5 events using a variational Bayesian In-  
486 dependent Component Analysis (vbICA) decomposition of the signal. As we

487 expect smaller magnitude events to be more visible at smaller time scales of the  
488 wavelet decomposition (level 5), we verify for all these events whether a signal  
489 can be seen at the same time as the time given in their catalog. Most of these  
490 magnitude 5 events are also sub-events of bigger magnitude 6 events. Table 2  
491 summarizes for each event its timing, its number and its magnitude as indi-  
492 cated in the catalog from Michel et al. [2019], and whether it is part of a bigger  
493 magnitude 6 event. Figure 10 shows the 5th level detail wavelet decomposition  
494 of the GPS data. Red lines show the timing of the big slow slip events from  
495 Table 1, and blue lines show the timing of the small slow slip events from Table 2.

496

497 All 14 events that are sub-events of a bigger event are visible at level 5.  
498 However, this may be because the bigger events are clearly seen at levels 6 to 8,  
499 and also at smaller time scales. The one small event that is not part of a bigger  
500 event (Winter 2009) is visible at level 5 of the wavelet decomposition. However,  
501 some other events that are not in the catalog of Michel et al. [2019]’s catalog  
502 are also visible in late 2007, early 2010, early 2012, and early 2020. Therefore,  
503 it is difficult to differentiate between a robust detection and a false detection,  
504 and to conclude whether the method can indeed detect events of magnitude 5.

505

506 In Figure 9, we see four smaller events that are not in the catalog of Michel  
507 et al. [2019]: at about 2007.5, there is a negative peak followed by a positive  
508 peak (that is an event in the opposite direction of what would be expected from  
509 slow slip), at about 2010.2, 2012.2 and 2020.2, there are positive peaks followed  
510 by negative peaks for all the sixteen locations studied in this paper. These  
511 events are highlighted in Figure S4 in the Supplementary Information. Looking  
512 back at the original GPS data, there is a small increase in the displacement  
513 in the eastern direction that lasts about one or two months at about 2007.5.

514 However, the direction of the displacement does not correspond to a slow slip  
515 event, and another cause should be found to explain this signal. There is a de-  
516 crease in displacement that lasts several months at about 2010.2. This transient  
517 may correspond to a long duration slow slip event. There is a small decrease  
518 in displacement at about 2012.2. Its amplitude is small but the duration and  
519 direction correspond to a slow slip event, so this transient could be a very small  
520 slow slip event. Finally, there is also a small decrease in displacement at about  
521 2020.2 that is difficult to interpret.

522

523 Due to the short distances between the GPS stations and the locations of the  
524 red triangles on the map from Figure 3, the same station could be used multiple  
525 times for the stacking at different locations. When considering two different lo-  
526 cations, the stacking is thus made over an overlapping number of stations. Table  
527 3 summarizes the number of stations and the number of overlapping stations for  
528 each location on Figure 3. We hypothesize that the small displacement in the  
529 eastern direction seen at about 2007.5 could be due to a misbehaving station  
530 common to several locations. However, several GPS stations indeed show an  
531 increase in the displacement in the eastern direction at about 2007.5. There are  
532 many missing data around that time, so it is difficult to conclude.

533

534 Another possibility is that common mode signals could stack constructively  
535 across GNSS stations and produce peaks in the wavelet details that are actually  
536 due to non-tectonic signals. We computed common mode signals for different  
537 latitude bins (each bin has width equal to half-a-degree of latitude) following  
538 the same method as Nuyen and Schmidt [2021]. We first stacked all the time  
539 series for the stations in each latitude bin that are located more than 100 km  
540 east of the 40 km depth contour of the plate boundary. We assume that these

541 stations are not sensitive to the deformation on the plate interface. We then  
542 apply a yearly moving average to each common mode signal in order to remove  
543 any leftover noise. The common mode signal was then removed from the GNSS  
544 time series depending on each sites latitude. Figure S3 in the Supplementary  
545 Information shows the corresponding sum of the stacks of the 6th, 7th and 8th  
546 wavelet details obtained from the resulting time series. The common modes  
547 seem to have little impact on the results and do not explain the additional four  
548 small events that we noted in Figure 9.

549

550 In order to convert our filtered eastward displacement time series into a slow  
551 slip event catalog we note that red bars represent displacements exceeding a  
552 threshold of 0.8 mm (east), and blue marks displacements less than minus -0.8  
553 mm (west). During times with no slow slip GPS stations on the overriding plate  
554 are pushed slowly eastward by the locked subducting plate. Slow slip events  
555 represent GPS motion **towards** the west. Thus, we infer that slow slip events  
556 happen when red bars are immediately followed by blue bars in the wavelet  
557 details. We have identified everywhere that this has happened and mark it with  
558 a green line in Figure 11 and as a row in Table 4. We find 17 possible SSEs  
559 by this method using filtered GPS data only. For each of these 17 events we  
560 determine the time difference between the mid time of the GPS catalog and the  
561 nearest time from the tremor catalog (Table 1). These time differences are in  
562 column 6 (Table 4). Every event in the GPS catalog has a match in the tremor  
563 catalog except for the tremor event at 2010.15. There is also only one event in  
564 the tremor catalog that is not in the GPS catalog. It occurs at 2014.65 with  
565 a duration of 15 days and 190 hours of tremor. It occurs 0.25 years after the  
566 nearest GPS event. There are also two marginal events in the tremor catalog  
567 with time differences of 0.13 and 0.10 years, but those are also among the smaller

568 events with 162 and 193 hours of tremor.

## 569 5 Application to data from New Zealand

570 We now apply our wavelet-based method to detect slow slip events in New  
571 Zealand, a location where **the spatial and temporal agreement between**  
572 **tremor and slow slip is not as good as in** other subduction zones. The  
573 tectonics of the North Island of New Zealand are dominated by the westward  
574 subduction of the Pacific Plate under the Australian Plate at the Hikurangi  
575 Trench. Two types of slow slip events have been observed at the Hikurangi  
576 margin. Shallow (10-15 km depth), shorter (1-3 weeks), and usually smaller  
577 (Mw 6.3-6.8) slow slip events have been observed every 18-24 months in the  
578 northern part of the margin. Deeper (35-60 km depth), longer (12-18 months),  
579 and larger (Mw 7.0) slow slip events have been observed every 5 years in the  
580 southern part of the margin [Wallace and Beavan, 2010, Todd and Schwartz,  
581 2016]. The detection of tremor has been elusive in northern Hikurangi. Dela-  
582 haye et al. [2009] observed an increase in the rate of microseismicity downdip of  
583 the 2004 Gisborne slow slip event. More recently, however, [Kim et al., 2011]  
584 detected a low level of tremor activity that increased during the 2010 Gisborne  
585 slow slip event. As was the case for the microearthquakes, the source of the  
586 tremor was located downdip of the slow slip patch determined from GNSS data.  
587 [Ide, 2012] detected tremor downdip of the location of two deep slow slip events  
588 observed by Wallace and Eberhart-Phillips [2013] in 2006 and 2008. However,  
589 contrary to ETS events in Cascadia and Nankai, the tremor activity did not  
590 seem to increase during the slow slip events. Todd and Schwartz [2016] de-  
591 tected tremor associated with most of the shallow slow slip events between 2010  
592 and 2015, and located downdip of the geodetically inferred slip area. They also  
593 detected deeper tremor between 20 and 50 km depth with unclear origin. They

594 hypothesized that these tremor may be related to undetected deep long-term  
595 slow slip events.

596

597 To evaluate whether the wavelet analysis is effective in a region without  
598 robust tremor, we take all the New Zealand GPS stations located in a 50 km  
599 radius of a given **location**, for the 18 locations indicated in Figure 12, and we  
600 stack the 6th level details, the 7th level details or the 8th level details over all  
601 the GPS stations. We then sum together the 6th, 7th and 8th levels stacked  
602 wavelet details (Figure 13, top panel). We highlight positive and negative peaks  
603 with red and blue colors as was done in Figure 9. We cannot use the tremor data  
604 to decide what is the appropriate threshold above which we consider that there  
605 is a slow slip event. **Slow slip events in New Zealand result in surface**  
606 **displacements that are similar in amplitude to twice as large as those**  
607 **observed in Cascadia.** Therefore, the amplitudes of the peaks in the wavelet  
608 details should be similar in New Zealand and in Cascadia and we choose iden-  
609 tical thresholds for both regions. As a slow slip event in northern New Zealand  
610 results in a displacement in the east direction at the earths surface, the slow  
611 slip events are indicated by a negative peak followed by a positive peak in the  
612 stacked wavelet details. We compare the results of the timings and locations of  
613 the slow slip events to those events detected by Todd and Schwartz [2016]. As  
614 they only used data from five GPS stations (PUKE, ANAU, GISB, MAHI and  
615 CKID), we indicate by a vertical orange bar on the bottom panel of Figure 13  
616 each time a slow slip event was detected for these stations. The orange bars are  
617 centered on the latitudes of the GPS stations. If a slow slip event was detected  
618 by more than one station, all the corresponding orange bars are linked together  
619 to show the spatial extent of the slow slip. Todd and Schwartz [2016] indicated  
620 by a question mark (on their Figure 2 and their Table 1) additional possible

621 events, and those are indicated by a dotted orange bar on Figure 13. To com-  
622 pare with the slow slip events detected with the wavelet method, we also mark  
623 by a green bar every time a negative peak lower than the threshold is followed  
624 by a positive peak higher than the threshold. Table 5 summarizes the slow slip  
625 events detected with the wavelet method for 2010-2016.

626

627 We observe that there is a good **agreement** between the events detected  
628 with the wavelet method and the events previously detected by Todd and  
629 Schwartz [2016]. We clearly see an event propagating from south to north  
630 in January-February (event 2 from Todd and Schwartz [2016]), an event in  
631 March-April 2010 (event 3), an event in April-May 2011 in the northern part  
632 of the region studied (events 6 and 7), an event propagating south-to-north in  
633 August-September and September-October 2011 (events 8 and 9), and an event  
634 in December 2011 (event 10). Although Todd and Schwartz [2016] only de-  
635 tected this last event for GPS station GISB, it seems that this event may have  
636 also extended farther to the north and the south. We then clearly see an event  
637 in the northern part of the region studied in August 2012 (event 12), an event  
638 in December 2012-January 2013 (event 13), an event in the southern part of  
639 the region studied in February-March 2013 (event 14), an event propagating  
640 from south to north in June-July and July-August 2013 (events 15 and 16), an  
641 event in September 2014 (events 20 and 21), an event in the southern part of  
642 the region studied in December 2014-January 2015 (events 22 and 23), and an  
643 event in June-July 2015 in the northern part of the region studied (event 26).  
644 It is unclear if the event near station ANAU in early 2010 (event 1) is visible  
645 in the wavelet details as it is too close to the beginning of the time series. The  
646 June-July 2010 event (event 4), the August 2010 event (event 5), and the March  
647 2012 event (event 11), are not clearly visible in the wavelet details. The events

648 in September-October 2013 (event 17), December 2013 (event 18), May-June  
649 2014 (event 19), January-February (event 24) and February 2015 (events 25)  
650 are not clearly seen in the wavelet details, but there could be a small negative  
651 peak followed by a small positive peak at these times. Additionally, there could  
652 be two other events that are not in [Todd and Schwartz, 2016] in Fall 2010  
653 (southern part of the region studied) and in Fall 2015.

654

655 Our wavelet-based method thus works well to detect transients in GPS data  
656 that could be slow slip events, even in the absence of tremor data. The choice  
657 of the appropriate threshold to decide that there is a transient and the levels  
658 of the wavelet details that we look at for the detection may still not be easily  
659 made. There is a difference between Cascadia and New Zealand in terms of  
660 which wavelet details to stack. In particular, as there is more time between  
661 two slow slip events in New Zealand than in Cascadia, the biggest slow slip  
662 events (early 2010, late 2011, 2013 and late 2014) can also be **seen** on the 9th  
663 level detail for New Zealand, whereas they could not be seen for Cascadia. We  
664 then use the method to detect slow slip events during the period 2016-2022,  
665 which was not covered by Todd and Schwartz [2016] (Figure 14). We note four  
666 large transients that could be slow slip events in late 2016, late 2017, early 2019  
667 and mid-2021. There are also possible smaller events in the northern part of  
668 the area in mid-2018 and in most of the area studied in early 2020. Table 6  
669 summarizes the slow slip events detected with the wavelet method for 2016-2022.

670

671 **The method is thus applicable in regions where tremor data are**  
672 **not usable. To determine which wavelet levels to stack, we recom-**  
673 **mend analyzing each level detail. Look for spatially coherent pat-**  
674 **terns, wavelet details with energy at similar times and high signal-**

675 to-noise ratios. Look for alternating positive and negative peaks that  
676 are consistent with the expected direction of slow slip. Consider  
677 wavelet details with time scales ranging from the expected duration  
678 of slow slip events to the expected recurrence times between slow slip  
679 events. For Cascadia and New Zealand this would be weeks to years.  
680 Determination of a threshold is subjective. At large thresholds the  
681 large slow slip events should be clear. At smaller thresholds there is  
682 the possibility of identifying smaller events, but at the risk of false  
683 detections.

## 684 6 Conclusion

685 In this paper, we develop and test a new approach for detecting transient events  
686 in GPS time series, such as slow slip events. We used wavelet methods to analyze  
687 GNSS time series and tremor recordings of slow slip events in Cascadia, and  
688 GNSS time series in New Zealand. We used detrended GNSS data, applied the  
689 MODWT transform, and stacked the wavelet details over several nearby GNSS  
690 stations. As an independent check on the timing of slow slip events, we also  
691 computed the cumulative number of tremor in the vicinity of the GNSS stations,  
692 detrended this signal, and applied the MODWT transform. In both time series,  
693 we could then see simultaneous waveforms whose timing corresponds to the  
694 timing of slow slip events. We assumed that there is a slow slip event whenever  
695 the wavelet signal gets above a threshold. We verified that there is a good  
696 **agreement** between slow slip events detected with only GNSS data, and slow  
697 slip events detected with only tremor data. The wavelet-based detection method  
698 detects all events of magnitude higher than 6 as determined by independent  
699 event catalogs (e.g. [Michel et al., 2019]). We detected signals in the GPS data  
700 that could be magnitude 5 events, but it is not easy to differentiate between

701 robust detections and false detections. We then applied the method to GNSS  
702 data in New Zealand and detected slow slip events consistent with the events  
703 previously detected by Todd and Schwartz [2016].

## 704 Data and Resources

705 The GPS recordings used for this analysis can be downloaded from the PANGA  
706 website [GPS/GNSS Network and Geodesy Laboratory: Central Washington  
707 University, other/seismic network, 1996] <http://www.panga.cwu.edu/> and the  
708 Geonet website <https://www.geonet.org.nz/>. The Python scripts used to  
709 analyze the data and make the figures can be found on the first author's Github  
710 account <https://github.com/ArianeDucellier/slowslip>. Figures 3 and 12  
711 were created using GMT [Wessel and Smith, 1991].

## 712 Acknowledgements

713 The authors would like to thank two anonymous reviewers and the Associate Ed-  
714 itor Jeanne Hardebeck, whose comments greatly helped improve the manuscript.  
715 This work was funded by the grant from the National Science Foundation EAR-  
716 1358512. A.D. would like to thank Professor Donald Percival for introducing  
717 her to wavelet methods during his excellent class on Wavelets: Data Analysis,  
718 Algorithms and Theory taught at University of Washington.

## 719 Declaration of Competing Interests

720 The authors declare no competing interests.

721 **References**

- 722 A.C. Aguiar, T.I. Melbourne, and C.W. Scrivner. Moment release rate of Cas-  
723 cadia tremor constrained by GPS. *J. Geophys. Res.*, 114:B00A05, 2009.
- 724 S. Alba, R. J. Weldon, D. Livelybrooks, and D. A. Schmidt. Cascadia ETS  
725 events seen in tidal records (1980–2011). *Bull. Seismol. Soc. Am.*, 109(2):  
726 812–821, 2019.
- 727 P. Audet and Y.H. Kim. Teleseismic constraints on the geological environment  
728 of deep episodic slow earthquakes in subduction zone forearcs: A review.  
729 *Tectonophysics*, 670:1–15, 2016.
- 730 N. M. Bartlow. A longterm view of episodic tremor and slip in Cascadia. *Geo-  
physical Research Letters*, 43(3):e2019GL085303, 2020.
- 732 G.C. Beroza and S. Ide. Slow earthquakes and nonvolcanic tremor. *Annu. Rev.  
Earth Planet. Sci.*, 39:271–296, 2011.
- 734 E.J. Delahaye, J. Townend, M.E. Reyners, and G. Rogers. Microseismicity but  
735 no tremor accompanying slow slip in the Hikurangi subduction zone, New  
736 Zealand. *Earth and Planetary Science Letters*, 277:21–28, 2009.
- 737 W.B. Frank. Slow slip hidden in the noise: The intermittence of tectonic release.  
738 *Geophys. Res. Lett.*, 43:10125–10133, 2016.
- 739 GPS/GNSS Network and Geodesy Laboratory: Central Washington University,  
740 other/seismic network. Pacific Northwest Geodetic Array (PANGA), 1996.  
741 URL <http://www.panga.cwu.edu/>.
- 742 K. Hall, H. Houston, and D. Schmidt. Spatial comparisons of tremor and slow  
743 slip as a constraint on fault strength in the northern Cascadia subduction  
744 zone. *Geochemistry, Geophysics, Geosystems*, 19(8):2706–2718, 2018.

- 745 J. C. Hawthorne and A. M. Rubin. Shorttime scale correlation between slow  
746 slip and tremor in Cascadia. *Journal of Geophysical Research: Solid Earth*,  
747 118:1316–1329, 2013.
- 748 Y. Hiramatsu, T. Watanabe, and K. Obara. Deep lowfrequency tremors as a  
749 proxy for slip monitoring at plate interface. *Geophysical Research Letters*, 35:  
750 L13304, 2008.
- 751 S. Ide. Variety and spatial heterogeneity of tectonic tremor worldwide. *Journal*  
752 *of Geophysical Research*, 117:B03302, 2012.
- 753 Y. Jiang, S. Wdowinski, T. H. Dixon, M. Hackl, M. Protti, and V. Gonzalez.  
754 Slow slip events in Costa Rica detected by continuous GPS observations,  
755 2002–2011. *Geochemistry, Geophysics, Geosystems*, 13:Q04006, 2012.
- 756 M.J. Kim, S.Y. Schwartz, and S. Bannister. Nonvolcanic tremor associated with  
757 the March 2010 Gisborne slow slip event at the Hikurangi subduction margin,  
758 New Zealand. *Geophysical Research Letters*, 38:L14301, 2011.
- 759 P. Kumar and E. Foufoula-Georgiou. Wavelet analysis for geophysical applica-  
760 tions. *Rev. Geophys.*, 35(4):385–412, 1997.
- 761 S. Li, J. Freymueller, and R. McCaffrey. Slow slip events and timedependent  
762 variations in locking beneath Lower Cook Inlet of the AlaskaAleutian sub-  
763 duction zone. *Journal of Geophysical Research: Solid Earth*, 121:1060–1079,  
764 2016.
- 765 S. Michel, A. Gualandi, and J.-P. Avouac. Interseismic coupling and slow slip  
766 events on the Cascadia megathrust. *Pure Appl. Geophys.*, 176:3867–3891,  
767 2019.
- 768 T. Nishimura, T. Matsuzawa, and K. Obara. Detection of shortterm slow slip

- 769 events along the Nankai Trough, southwest Japan, using GNSS data. *Journal*  
770 *of Geophysical Research: Solid Earth*, 118:3112–3125, 2013.
- 771 C. P. Nuyen and D. A. Schmidt. Filling the gap in Cascadia: The emergence of  
772 lowamplitude longterm slow slip. *Geochemistry, Geophysics, Geosystems*, 22  
773 (3):e2020GC009477, 2021.
- 774 K. Obara, H. Hirose, F. Yamamizu, and K. Kasahara. Episodic slow slip events  
775 accompanied by non-volcanic tremors in southwest Japan subduction zone.  
776 *Geophysical Research Letters*, 31:L23602, 2004.
- 777 R. Ohtani, J.J. McGuire, and P. Segall. Network strain filter: A new tool for  
778 monitoring and detecting transient deformation signals in GPS arrays. *J.*  
779 *Geophys. Res.*, 115:B12418, 2010.
- 780 D.B. Percival and A.T. Walden. *Wavelet Methods for Time Series Analysis*.  
781 Cambridge Series in Statistical and Probabilistic Mathematics. Cambridge  
782 University Press, New York, NY, USA, 2000.
- 783 L.A. Preston, K.C. Creager, R.S. Crosson, T.M. Brocher, and A.M. Trehu.  
784 Intraslab earthquakes: Dehydration of the Cascadia slab. *Science*, 302:1197–  
785 1200, 2003.
- 786 M. Radiguet, F. Cotton, M. Vergnolle, M. Campillo, A. Walpersdorf, N. Cotte,  
787 and V. Kostoglodov. Slow slip events and strain accumulation in the Guerrero  
788 gap, Mexico. *Journal of Geophysical Research: Solid Earth*, 117:B04305, 2012.
- 789 G. Rogers and H. Dragert. Tremor and slip on the Cascadia subduction zone:  
790 The chatter of silent slip. *Science*, 300(5627):1942–1943, 2003.
- 791 D. A. Schmidt and H. Gao. Source parameters and timedependent slip distribu-  
792 tions of slow slip events on the Cascadia subduction zone from 1998 to 2008.  
793 *Journal of Geophysical Research: Solid Earth*, 115:B00A18, 2010.

- 794 D.R. Shelly, G.C. Beroza, and S. Ide. Non-volcanic tremor and low-frequency  
795 earthquake swarms. *Nature*, 446:305–307, 2007.
- 796 W. Szeliga, T.I. Melbourne, M.M. Miller, and V.M. Santillan. Southern Casca-  
797 dia episodic slow earthquakes. *Geophys. Res. Lett.*, 31:L16602, 2004.
- 798 W. Szeliga, T. Melbourne, M. Santillan, and M. Miller. GPS constraints on 34  
799 slow slip events within the Cascadia subduction zone, 1997-2005. *J. Geophys.*  
800 *Res.*, 113:B04404, 2008.
- 801 E.K. Todd and S.Y. Schwartz. Tectonic tremor along the northern Hikurangi  
802 Margin, New Zealand, between 2010 and 2015. *J. Geophys. Res. Solid Earth*,  
803 121:8706–8719, 2016.
- 804 M. Vergnolle, A. Walpersdorf, V. Kostoglodov, P. Tregoning, J. A. Santiago,  
805 N. Cotte, and S. I. Franco. Slow slip events in Mexico revised from the  
806 processing of 11 year GPS observations. *Journal of Geophysical Research: Solid Earth*,  
807 115:B08403, 2010.
- 808 L. M. Wallace. Slow slip events in New Zealand. *Annual Review of Earth and*  
809 *Planetary Sciences*, 48:175–203, 2020.
- 810 L. M. Wallace, J. Beavan, S. Bannister, and C. Williams. Simultaneous longterm  
811 and shortterm slow slip events at the Hikurangi subduction margin, New  
812 Zealand: Implications for processes that control slow slip event occurrence,  
813 duration, and migration. *Journal of Geophysical Research: Solid Earth*, 117:  
814 B11402, 2012.
- 815 L.M. Wallace and J. Beavan. Diverse slow slip behavior at the Hikurangi sub-  
816 duction margin, New Zealand. *Journal of Geophysical Research*, 115:B12402,  
817 2010.

- 818 L.M. Wallace and D. Eberhart-Phillips. Newly observed, deep slow slip events  
819 at the central Hikurangi margin, New Zealand: Implications for downdip vari-  
820 ability of slow slip and tremor, and relationship to seismic structure. *Geo-*  
821 *physical Research Letters*, 40:5393–5398, 2013.
- 822 A.G. Wech. Interactive tremor monitoring. *Seismol. Res. Lett.*, 81(4):664–669,  
823 2010.
- 824 A.G. Wech. Extending Alaska’s plate boundary; tectonic tremor generated by  
825 Yakutat subduction. *Geology*, 44(7):587–590, 2016.
- 826 M. Wei, J.J. McGuire, and E. Richardson. A slow slip event in the south central  
827 Alaska Subduction Zone. *Geophys. Res. Lett.*, 39:L15309, 2012.
- 828 P. Wessel and W. H. F. Smith. Free software helps map and display data. *EOS*  
829 *Trans. AGU*, 72:441, 1991.
- 830 C. A. Williams, D. Eberhart-Phillips, S. Bannister, D. H. Barker, S. Henrys,  
831 M. Reyners, and R. Sutherland. Revised interface geometry for the Hikurangi  
832 subduction zone, New Zealand. *Seismological Research Letters*, 84(6):1066–  
833 1073, 2013.

<sup>834</sup> **Addresses**

<sup>835</sup> Ariane Ducellier. University of Washington, Department of Earth and Space  
<sup>836</sup> Sciences, Box 351310, 4000 15th Avenue NE Seattle, WA 98195-1310.

<sup>837</sup>

<sup>838</sup> Kenneth C. Creager. University of Washington, Department of Earth and  
<sup>839</sup> Space Sciences, Box 351310, 4000 15th Avenue NE Seattle, WA 98195-1310.

<sup>840</sup>

<sup>841</sup> David A. Schmidt. University of Washington, Department of Earth and  
<sup>842</sup> Space Sciences, Box 351310, 4000 15th Avenue NE Seattle, WA 98195-1310.

## Tables

Table 1: Episodic Tremor and Slip events with  $M > 6$  identified by MODWT in both the GPS and the tremor data. The duration and the number of tremor are from the tremor catalog of the PNSN. The event number and the magnitude are from the slow slip catalog of Michel et al. [2019].

Time	Duration (days)	Number of tremor (hours)	Event number	Magnitude
2007.06	28	398	3	6.68
2008.36	25	402	10	6.56
2009.35	24	248	16	6.49
2010.63	29	518	24	6.54
2011.60	37	479	30	6.47
2012.72	37	620	34	6.54
2013.71	27	423	41	6.58
2014.65	15	190	48	6.03
2014.89	38	385	51	6.40
2016.11	43	421	54	6.79
2017.23	19	279	59	6.61
2018.49	22	381		
2019.23	34	195		
2019.88	16	205		
2020.79	26	193		
2020.86	12	162		
2021.09	14	230		

Table 2: Magnitude **5 to 6** events from Michel et al. [2019].

Time	Event number	Magnitude	Sub-event of bigger event
2007.06	1	5.64	Yes
2007.08	2	5.91	Yes
2008.38	11	5.50	Yes
2009.16	14	5.50	No
2009.36	17	5.32	Yes
2010.63	25	5.76	Yes
2011.66	31	5.61	Yes
2011.66	32	5.32	Yes
2012.69	35	5.56	Yes
2013.74	42	5.71	Yes
2014.69	49	5.31	Yes
2014.93	52	5.39	Yes
2016.03	57	5.80	Yes
2017.13	60	5.43	Yes
2017.22	61	5.37	Yes

Table 3: Number of GPS stations used for the stacking for each location on Figure 3 and number of common stations with the location immediately to the north and the location immediately to the south.

Index	Latitude	Number of stations	Common stations (north)	Common stations (south)
0	47.2	15	14	
1	47.3	18	17	14
2	47.4	24	20	17
3	47.5	21	20	20
4	47.6	22	14	20
5	47.7	17	12	14
6	47.8	13	8	12
7	47.9	10	9	8
8	48.0	10	7	9
9	48.1	8	7	7
10	48.2	10	8	7
11	48.3	9	9	8
12	48.4	9	5	9
13	48.5	7	5	5
14	48.6	6	5	5
15	48.7	5		5

Table 4: Cascadia catalog of slow slip events based only on MODWT analysis of GPS time series and inferring that the transition of red followed immediate by blue marks a slow slip event. First four columns are the start and end times and start and end latitudes of the green bars in Figure 11. The fifth column is 1 for robust detection and 2 if not as robust. Column 6 is the time difference in years between the mid times of the GPS catalog and the nearest mid times of the tremor catalog summarized in Table 1.

start time	end time	start latitude	end latitude	dT	tremor catalog
2007.06	2007.10	47.16	48.72	1	0.02
2008.30	2008.40	47.35	48.73	1	0.01
2009.35	2009.44	47.92	48.73	1	0.05
2010.12	2010.15	47.32	48.73	1	0.50 no match
2010.61	2010.64	47.17	48.72	1	0.00
2011.57	2011.61	47.18	48.68	1	0.01
2012.65	2012.65	48.74	47.76	1	0.05
2013.71	2013.75	47.47	48.73	1	0.02
2014.89	2014.90	48.73	47.79	1	0.01
2015.98	2016.09	48.73	47.20	1	0.08
2017.17	2017.24	47.38	48.72	1	0.02
2018.35	2018.36	47.48	47.93	1	0.13 part of same event?
2018.48	2018.50	48.72	48.09	1	0.00
2019.32	2019.34	47.17	47.72	2	0.10
2019.90	2019.91	48.47	48.72	2	0.02
2020.79	2020.83	47.18	48.13	1	0.02 & 0.05
2021.11	2021.12	48.75	48.48	2	0.02

Table 5: New Zealand catalog of slow slip events for 2010-2016 based only on MODWT analysis of GPS time series and inferring that the transition of red followed immediate by blue marks a slow slip event. First four columns are the start and end times and start and end latitudes of the green bars in Figure 13. The fifth column is 1 for robust detection and 2 if not as robust.

start time	end time	start latitude	end latitude	
2010.05	2010.07	-39.67	-39.12	1
2010.19	2010.22	-39.12	-38.07	1
2010.75	2010.76	-39.73	-39.41	1
2011.36	2011.37	-38.22	-38.02	2
2011.71	2011.74	-37.97	-38.41	1
2011.67	2011.71	-39.73	-38.91	1
2011.92	2011.95	-38.84	-38.16	1
2012.63	2012.63	-39.42	-39.62	2
2012.64	2012.66	-38.53	-38.02	1
2012.95	2012.96	-38.32	-37.98	1
2013.15	2013.16	-38.87	-39.72	1
2013.55	2013.57	-38.62	-38.01	1
2013.74	2013.74	-38.77	-38.97	2
2013.92	2013.93	-38.17	-37.98	2
2013.91	2013.95	-39.37	-39.73	1
2014.78	2014.79	-38.03	-39.03	1
2014.96	2015.00	-39.07	-39.72	1
2015.53	2015.53	-39.42	-39.72	1
2015.52	2015.55	-37.97	-38.43	1
2015.78	2015.79	-38.77	-39.37	1

Table 6: New Zealand catalog of slow slip events for 2016-2022 based only on MODWT analysis of GPS time series and inferring that the transition of red followed immediate by blue marks a slow slip event. First four columns are the start and end times and start and end latitudes of the green bars in Figure 13.

The fifth column is 1 for robust detection and 2 if not as robust.

start time	end time	start latitude	end latitude	
2016.84	2016.90	-37.96	-39.72	1
2017.10	2017.10	-38.78	-39.00	2
2017.73	2017.78	-37.98	-38.51	1
2018.04	2018.06	-38.58	-39.07	1
2018.63	2018.64	-38.27	-37.97	2
2019.26	2019.33	-37.97	-39.73	1
2020.09	2020.12	-37.97	-38.23	2
2020.34	2020.35	-37.96	-39.72	1
2020.33	2020.33	-37.96	-38.10	2
2020.32	2020.32	-38.62	-38.79	2
2020.36	2020.37	-39.70	-39.35	2
2021.11	2021.11	-39.51	-39.64	2
2021.39	2021.47	-39.72	-38.08	1

844 **Figure captions**

- 845 • Figure 1. Demonstration of a wavelet decomposition for a synthetic dataset.  
846 A synthetic time series is created (top row) with steps of period 500 days,  
847 and transient durations of 2 days (left), 5 days, 10 days, and 20 days  
848 (right). The resulting details and smooths are shown in increasing level.  
849 The amplitude of the synthetic time series is normalized to 1, and the  
850 details and smooths show the relative amplitude.
- 851 • Figure 2. Top left: **East-west** displacement recorded at GPS station  
852 PGC5. The resulting details and smooth of the wavelet decomposition  
853 are shown in increasing level from top to bottom and from left to right.
- 854 • Figure 3. GPS stations used in this study (black triangles). The black  
855 line represents the 40 km depth contour of the plate boundary model by  
856 Preston et al. [2003]. The red triangles are the locations where we stack  
857 the GPS data. The small grey dots are all the tremor locations from the  
858 PNSN catalog.
- 859 • Figure 4. Details and smooth of the wavelet decomposition of the de-  
860 trended cumulative tremor count around the third northernmost red tri-  
861 angles on Figure 3 (latitude 48.5).
- 862 • Figure 5. Top: Stacked 8th level details of the wavelet decomposition of  
863 the displacement over all the GPS stations located in a 50 km radius of a  
864 given point, for the 16 red triangles indicated in Figure 3. Bottom: 8th  
865 level detail multiplied by -1 of the cumulative tremor count in a 50 km  
866 radius of a given point for the same 16 locations. The black lines represent  
867 the timings of the ETS events from Table 1. We mark by a red rectangle  
868 every time where the amplitude is higher than a threshold of 0.4 mm (for  
869 the GPS) or 0.003 (for the tremor, **that is about 17 times the average**

870       **value of the signal)**. We mark by a blue rectangle every time where the  
871       amplitude is lower than minus the threshold.

- 872     ● Figure 6. Top: Stacked 7th level details of the wavelet decomposition of  
873       the displacement over all the GPS stations located in a 50 km radius of a  
874       given point, for the 16 red triangles indicated in Figure 3. Bottom: 7th  
875       level detail multiplied by -1 of the cumulative tremor count in a 50 km  
876       radius of a given point for the same 16 locations. The black lines represent  
877       the timings of the ETS events from Table 1. We mark by a red rectangle  
878       every time where the amplitude is higher than a threshold of 0.5 mm (for  
879       the GPS) or 0.01 (for the tremor, **that is about 56 times the average**  
880       **value of the signal)**. We mark by a blue rectangle every time where the  
881       amplitude is lower than minus the threshold.
- 882     ● Figure 7. Top: Stacked 6th level details of the wavelet decomposition of  
883       the displacement over all the GPS stations located in a 50 km radius of a  
884       given point, for the 16 red triangles indicated in Figure 3. Bottom: 6th  
885       level detail multiplied by -1 of the cumulative tremor count in a 50 km  
886       radius of a given point for the same 16 locations. The black lines represent  
887       the timings of the ETS events from Table 1. We mark by a red rectangle  
888       every time where the amplitude is higher than a threshold of 0.3 mm (for  
889       the GPS) or 0.009 (for the tremor, **that is about 51 times the average**  
890       **value of the signal)**. We mark by a blue rectangle every time where the  
891       amplitude is lower than minus the threshold.
- 892     ● Figure 8. ROC curve for the sum of the 6th, 7th, and 8th level details  
893       of the wavelet decomposition. Each dot represents the true positive rate  
894       of event detections and the false positive rate of event detections for a  
895       given pair of thresholds (for the GPS and for the tremor). The black  
896       cross marks the true positive rate and the false positive rate obtained

897 with the thresholds used to make Figure 9. The values of the threshold  
898 are color-coded. Reds (bottom curve) correspond to the lowest value of  
899 the threshold for the tremor (0.001), while oranges, greens, blues, purples  
900 correspond to increasing values of the threshold for the tremor (up to 0.01,  
901 top curve). The brightest colors (bottom left) correspond to the highest  
902 values of the threshold for the GPS (1.5 mm), while the darker colors (top  
903 right) correspond to decreasing values of the threshold for the GPS (0.1  
904 mm).

- 905 • Figure 9. Top: Stacked sum of the 6th, 7th and 8th levels details of  
906 the wavelet decomposition of the displacement over all the GPS stations  
907 located in a 50 km radius of a given point, for the 16 red triangles indicated  
908 in Figure 3. Bottom: Sum of the 6th, 7th and 8th levels detail multiplied  
909 by -1 of the cumulative tremor count in a 50 km radius of a given point  
910 for the same 16 locations. The black lines represent the timings of the  
911 ETS events from Table 1. We mark by a red rectangle every time where  
912 the amplitude is higher than a threshold of 0.8 mm (for the GPS) or 0.01  
913 (for the tremor, **that is about 56 times the average value of the**  
914 **signal**). We mark by a blue rectangle every time where the amplitude is  
915 lower than minus the threshold.
- 916 • Figure 10. Top: Stacked 5th level details of the wavelet decomposition  
917 of the displacement over all the GPS stations located in a 50 km radius  
918 of a given point, for the 16 red triangles indicated in Figure 3. The red  
919 lines represent the timings of the ETS events from Table 1. The blue  
920 lines represent the timings of the magnitude 5 events from the catalog of  
921 Michel et al. [2019].
- 922 • Figure 11. Same as top panel of Figure 9: Stacked sum of the 6th, 7th  
923 and 8th levels details of the wavelet decomposition of the displacement

924 over all the GPS stations located in a 50 km radius of a given point, for  
925 the 16 red triangles indicated in Figure 3. We mark with a green bar the  
926 slow slip events from Table 4 detected with the wavelet method. Full lines  
927 correspond to robust detections (1 in Table 4) and dotted lines to less  
928 robust detections (2 in Table 4).

- 929 • Figure 12. GPS stations used for the slow slip detection in New Zealand  
930 (black triangles). The red triangles are the locations where we stack the  
931 GPS data. They are located close to the 20 km depth contour of the plate  
932 boundary from Williams et al. [2013].
- 933 • Figure 13. Top: Sum of the stacked 6th, 7th and 8th level details of  
934 the wavelet decomposition of the displacement over all the GPS stations  
935 located in a 50 km radius of a given point, for the 18 red triangles indicated  
936 in Figure 12. The time period covered is 2010-2016. We mark by a red  
937 rectangle every time where the amplitude is higher than a threshold equal  
938 to 0.8 mm. We mark by a blue rectangle every time where the amplitude  
939 is lower than minus the threshold. Bottom: Sum of the stacked 6th, 7th  
940 and 8th level details of the wavelet decomposition. We mark with an  
941 orange bar the slow slip events detected by Todd and Schwartz [2016]  
942 and with a green bar the slow slip events from Table 5 detected with the  
943 wavelet method. Full lines correspond to robust detections (1 in Table 5)  
944 and dotted lines to less robust detections (2 in Table 5).
- 945 • Figure 14. Top: Sum of the stacked 6th, 7th and 8th level details of  
946 the wavelet decomposition of the displacement over all the GPS stations  
947 located in a 50 km radius of a given point, for the 18 red triangles indicated  
948 in Figure 12. The time period covered in 2016-2022. We mark by a red  
949 rectangle every time where the amplitude is higher than a threshold equal  
950 to 0.8 mm. We mark by a blue rectangle every time where the amplitude

951       is lower than minus the threshold. We mark with a green bar the slow  
952       slip events from Table 6 detected with the wavelet method. Full lines  
953       correspond to robust detections (1 in Table 6) and dotted lines to less  
954       robust detections (2 in Table 6).

<sub>955</sub> **Figures**

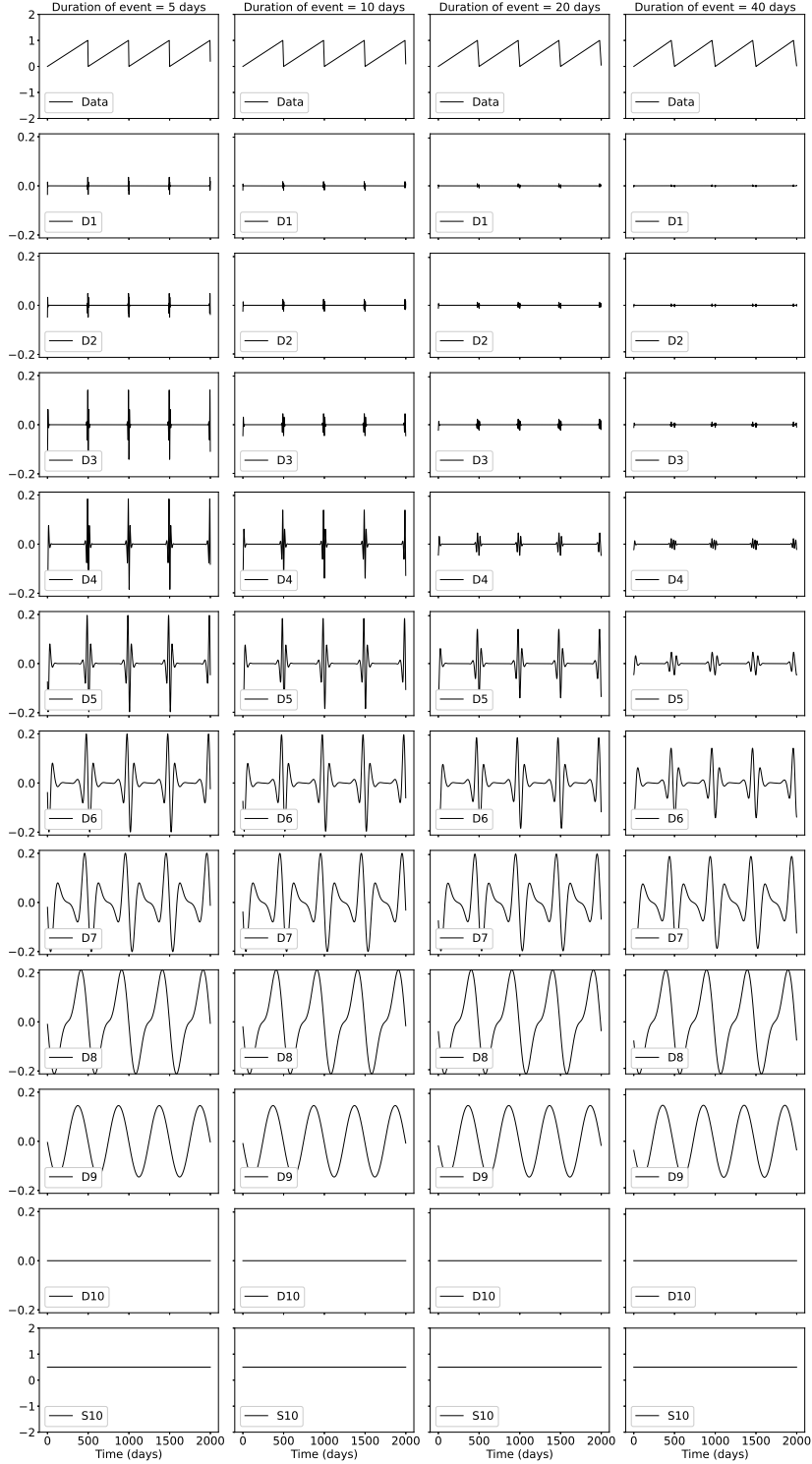


Figure 1: Demonstration of a wavelet decomposition for a synthetic dataset. A synthetic time series is created (top row) with steps of period 500 days, and transient durations of 2 days (left), 5 days, 10 days, and 20 days (right). The resulting details and smooths are shown in increasing level. The amplitude of the synthetic time series is normalized to 1, and the details and smooths show the relative amplitude. <sup>46</sup>

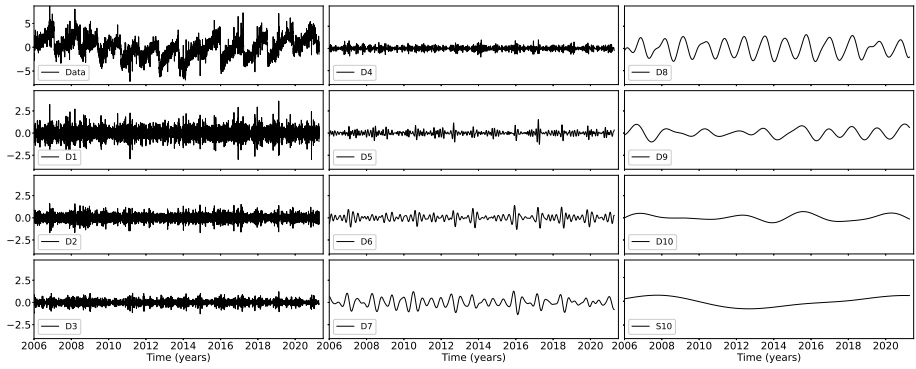


Figure 2: Top left: **East-west** displacement recorded at GPS station PGC5. The resulting details and smooth of the wavelet decomposition are shown in increasing level from top to bottom and from left to right.

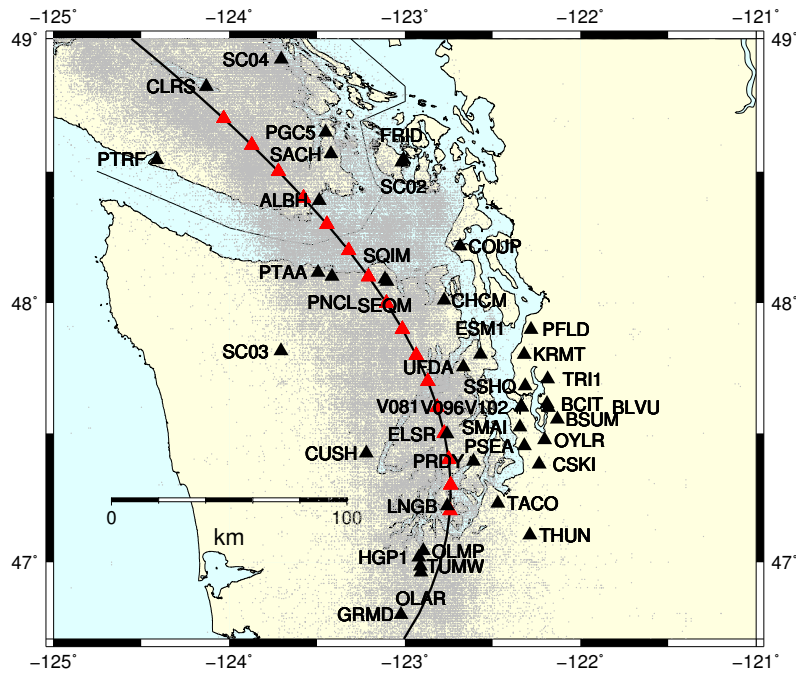


Figure 3: GPS stations used in this study (black triangles). The black line represents the 40 km depth contour of the plate boundary model by Preston et al. [2003]. The red triangles are the locations where we stack the GPS data. The small grey dots are all the tremor locations from the PNSN catalog.

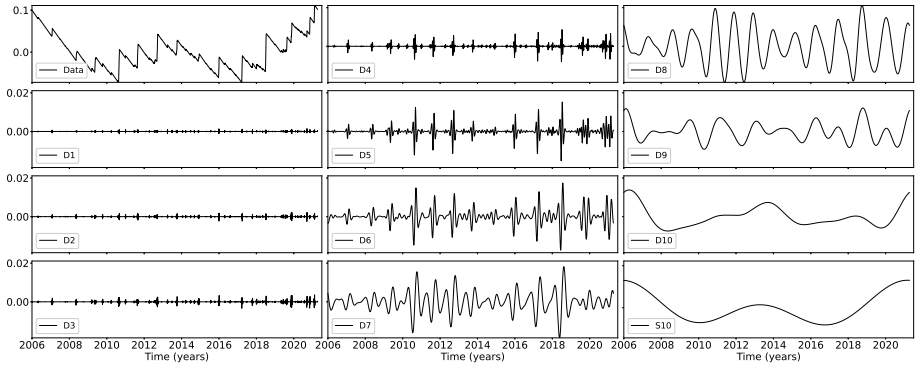


Figure 4: Details and smooth of the wavelet decomposition of the detrended cumulative tremor count around the third northernmost red triangles on Figure 3 (latitude 48.5).

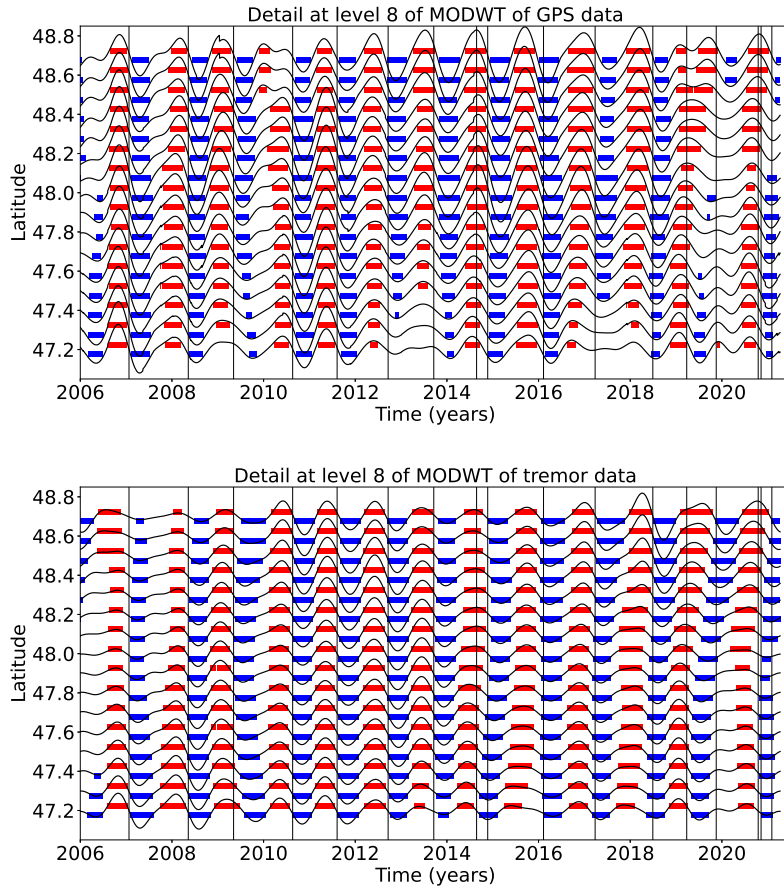


Figure 5: Top: Stacked 8th level details of the wavelet decomposition of the displacement over all the GPS stations located in a 50 km radius of a given point, for the 16 red triangles indicated in Figure 3. Bottom: 8th level detail multiplied by -1 of the cumulative tremor count in a 50 km radius of a given point for the same 16 locations. The black lines represent the timings of the ETS events from Table 1. We mark by a red rectangle every time where the amplitude is higher than a threshold of 0.4 mm (for the GPS) or 0.003 (for the tremor, **that is about 17 times the average value of the signal**). We mark by a blue rectangle every time where the amplitude is lower than minus the threshold.

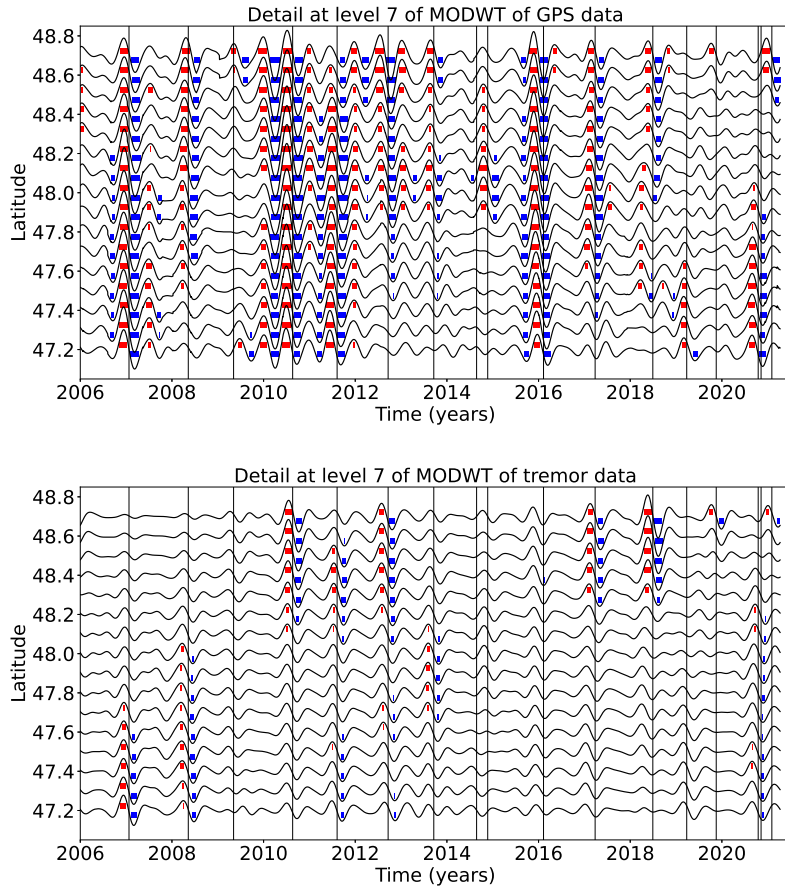


Figure 6: Top: Stacked 7th level details of the wavelet decomposition of the displacement over all the GPS stations located in a 50 km radius of a given point, for the 16 red triangles indicated in Figure 3. Bottom: 7th level detail multiplied by -1 of the cumulative tremor count in a 50 km radius of a given point for the same 16 locations. The black lines represent the timings of the ETS events from Table 1. We mark by a red rectangle every time where the amplitude is higher than a threshold of 0.5 mm (for the GPS) or 0.01 (for the tremor, **that is about 56 times the average value of the signal**). We mark by a blue rectangle every time where the amplitude is lower than minus the threshold.

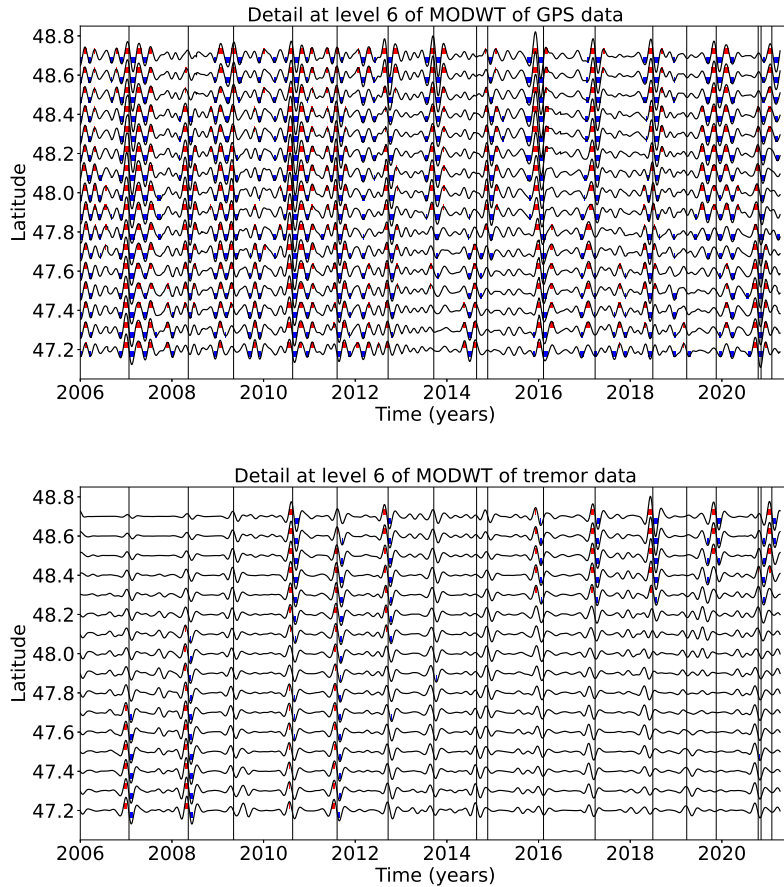


Figure 7: Top: Stacked 6th level details of the wavelet decomposition of the displacement over all the GPS stations located in a 50 km radius of a given point, for the 16 red triangles indicated in Figure 3. Bottom: 6th level detail multiplied by -1 of the cumulative tremor count in a 50 km radius of a given point for the same 16 locations. The black lines represent the timings of the ETS events from Table 1. We mark by a red rectangle every time where the amplitude is higher than a threshold of 0.3 mm (for the GPS) or 0.009 (for the tremor, **that is about 51 times the average value of the signal**). We mark by a blue rectangle every time where the amplitude is lower than minus the threshold.

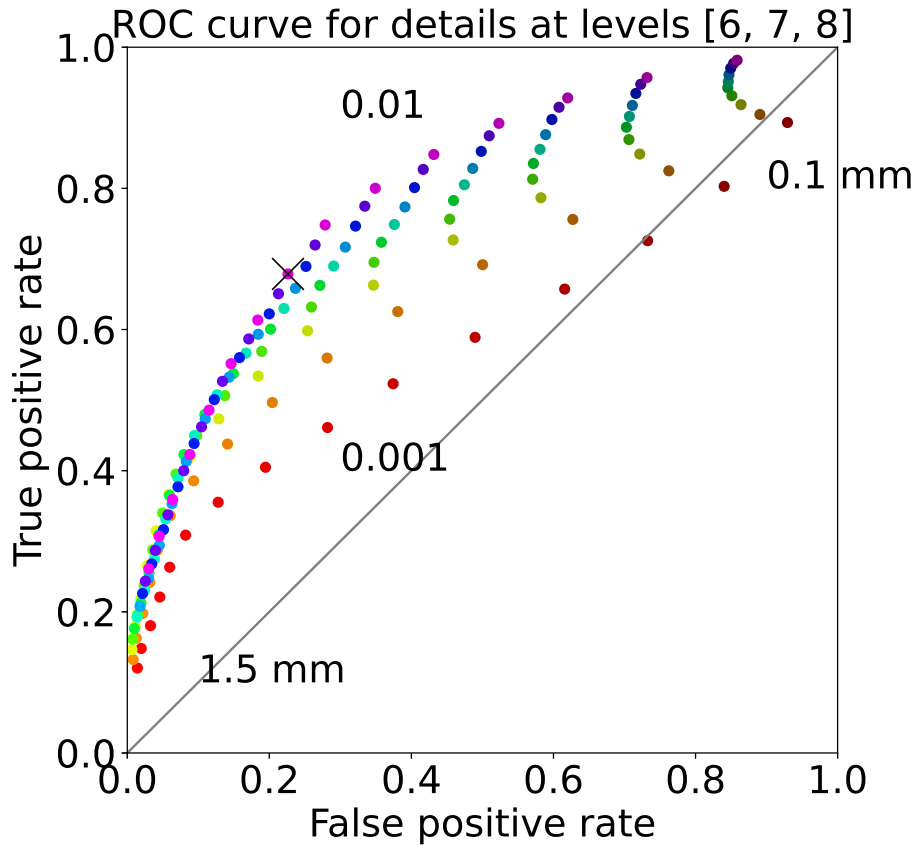


Figure 8: ROC curve for the sum of the 6th, 7th, and 8th level details of the wavelet decomposition. Each dot represents the true positive rate of event detections and the false positive rate of event detections for a given pair of thresholds (for the GPS and for the tremor). The black cross marks the true positive rate and the false positive rate obtained with the thresholds used to make Figure 9. The values of the threshold are color-coded. Reds (bottom curve) correspond to the lowest value of the threshold for the tremor (0.001), while oranges, greens, blues, purples correspond to increasing values of the threshold for the tremor (up to 0.01, top curve). The brightest colors (bottom left) correspond to the highest values of the threshold for the GPS (1.5 mm), while the darker colors (top right) correspond to decreasing values of the threshold for the GPS (0.1 mm).

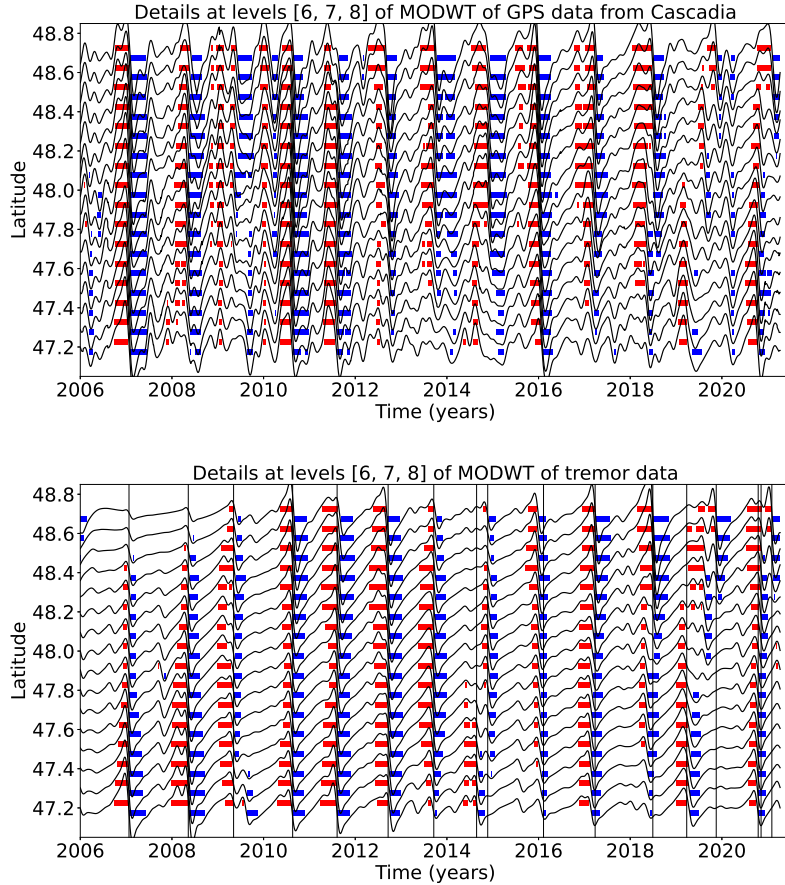


Figure 9: Top: Stacked sum of the 6th, 7th and 8th levels details of the wavelet decomposition of the displacement over all the GPS stations located in a 50 km radius of a given point, for the 16 red triangles indicated in Figure 3. Bottom: Sum of the 6th, 7th and 8th levels detail multiplied by -1 of the cumulative tremor count in a 50 km radius of a given point for the same 16 locations. The black lines represent the timings of the ETS events from Table 1. We mark by a red rectangle every time where the amplitude is higher than a threshold of 0.8 mm (for the GPS) or 0.01 (for the tremor, **that is about 56 times the average value of the signal**). We mark by a blue rectangle every time where the amplitude is lower than minus the threshold.

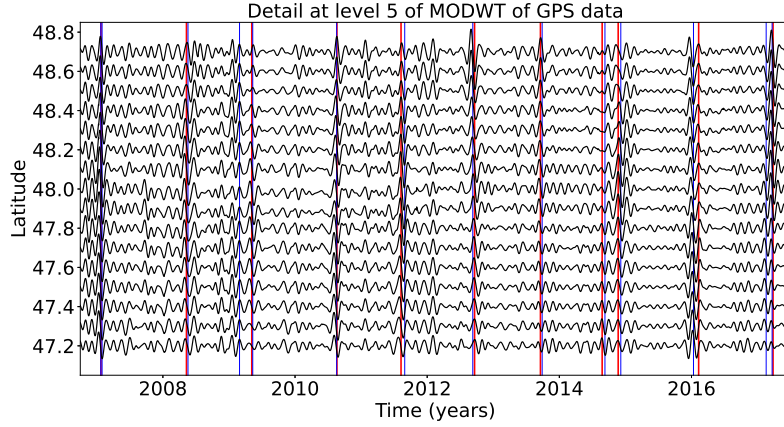


Figure 10: Top: Stacked 5th level details of the wavelet decomposition of the displacement over all the GPS stations located in a 50 km radius of a given point, for the 16 red triangles indicated in Figure 3. The red lines represent the timings of the ETS events from Table 1. The blue lines represent the timings of the magnitude 5 events from the catalog of Michel et al. [2019].

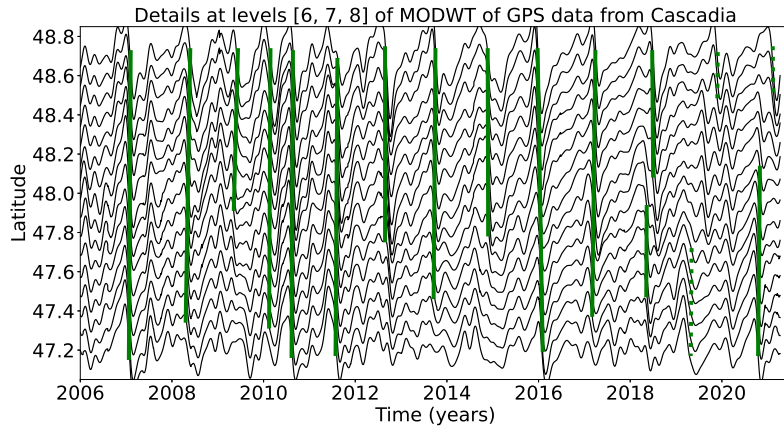


Figure 11: Same as top panel of Figure 9: Stacked sum of the 6th, 7th and 8th levels details of the wavelet decomposition of the displacement over all the GPS stations located in a 50 km radius of a given point, for the 16 red triangles indicated in Figure 3. We mark with a green bar the slow slip events from Table 4 detected with the wavelet method. Full lines correspond to robust detections (1 in Table 4) and dotted lines to less robust detections (2 in Table 4).

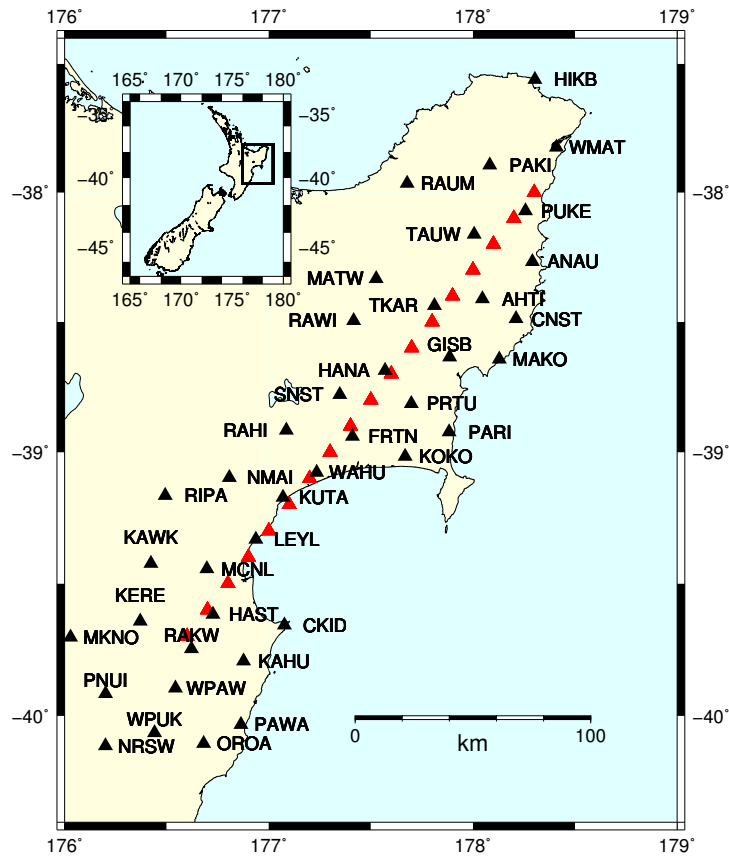


Figure 12: GPS stations used for the slow slip detection in New Zealand (black triangles). The red triangles are the locations where we stack the GPS data. They are located close to the 20 km depth contour of the plate boundary from Williams et al. [2013].

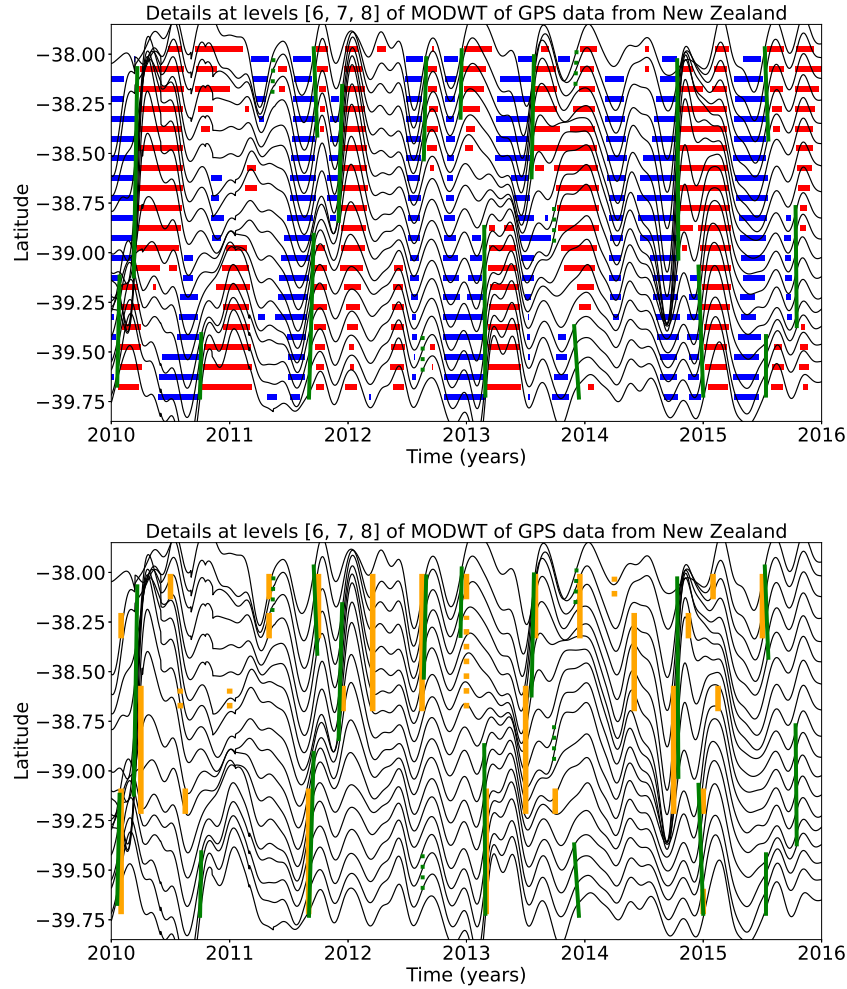


Figure 13: Top: Sum of the stacked 6th, 7th and 8th level details of the wavelet decomposition of the displacement over all the GPS stations located in a 50 km radius of a given point, for the 18 red triangles indicated in Figure 12. The time period covered is 2010-2016. We mark by a red rectangle every time where the amplitude is higher than a threshold equal to 0.8 mm. We mark by a blue rectangle every time where the amplitude is lower than minus the threshold. Bottom: Sum of the stacked 6th, 7th and 8th level details of the wavelet decomposition. We mark with an orange bar the slow slip events detected by Todd and Schwartz [2016] and with a green bar the slow slip events from Table 5 detected with the wavelet method. Full lines correspond to robust detections (1 in Table 5) and dotted lines to less robust detections (2 in Table 5).

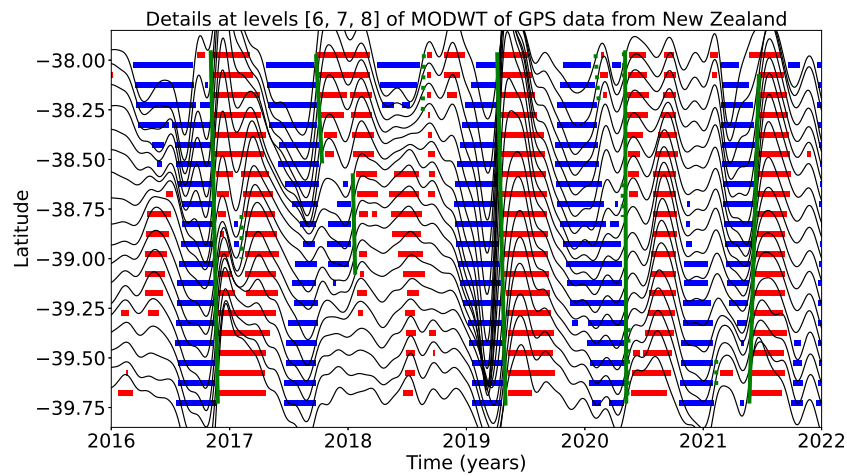


Figure 14: Top: Sum of the stacked 6th, 7th and 8th level details of the wavelet decomposition of the displacement over all the GPS stations located in a 50 km radius of a given point, for the 18 red triangles indicated in Figure 12. The time period covered in 2016-2022. We mark by a red rectangle every time where the amplitude is higher than a threshold equal to 0.8 mm. We mark by a blue rectangle every time where the amplitude is lower than minus the threshold. We mark with a green bar the slow slip events from Table 6 detected with the wavelet method. Full lines correspond to robust detections (1 in Table 6) and dotted lines to less robust detections (2 in Table 6).